ENG. Struct. Civ. Eng.
https://doi.org/10.1007/s11709-026-1365-x

RESEARCH ARTICLE

# Evaluation and prediction of self-healing performance of ultra-high-performance concrete based on the entropy weight method and response surface methodology

**Mingfeng DU[a], Meifeng DAI[a], Yongtao WANG[a], Xinru LI[a], Xin ZHANG[a], Xiaoying ZHUANG[b,c], Shuai ZHOU[a,d*]**

[a] *College of Materials Science and Engineering, Chongqing University, Chongqing 400045, China*
[b] *Department of Mathematics and Physics, Leibniz Universität Hannover, Hannover 30167, Germany*
[c] *Department of Geotechnical Engineering, College of Civil Engineering, Tongji University, Shanghai 200092, China*
[d] *State Key Laboratory of Safety and Resilience of Civil Engineering in Mountain Area, Chongqing University, Chongqing 400045, China*
[*] *Corresponding author. E-mail: shuaizhou@cqu.edu.cn*

© The Author(s) 2026. This article is published with open access at link.springer.com and journal.hep.com.cn

**ABSTRACT** To enhance the autogenous self-healing capacity of ultra-high-performance concrete (UHPC) from the perspective of mix proportion design, this study systematically investigates the effects of ground granulated blast furnace slag (GGBS), silica fume (SF), and steel fibers on the self-healing behavior of UHPC under water immersion conditions based on the response surface methodology. Multiple quantitative evaluation indicators were adopted and combined with the entropy weight method to construct a comprehensive scoring system, thereby realizing the objective evaluation of self-healing performance for different mix proportions. Then, regression models capable of predicting compressive strength, flexural strength, and the comprehensive score of self-healing performance were established. The results indicate that the self-healing of UHPC exhibits significant time dependence. The self-healing products are mainly composed of carbonate deposits and secondary hydration products. Increasing the contents of steel fibers and SF can effectively enhance the compressive and flexural strengths of UHPC. Elevating the GGBS dosage is more conducive to improving the self-healing performance, and there exists a significant positive synergistic effect between GGBS and steel fibers. The established models demonstrate good fit and reliable predictive ability. This study provides support for the development of UHPC with excellent self-healing performance.

**KEYWORDS** UHPC, autogenous self-healing, response surface methodology, entropy weight method

## 1 Introduction

Ultra-high-performance concrete (UHPC) is an emerging class of cementitious composites. Owing to its ultra-high strength, high toughness, and excellent durability, UHPC has been widely adopted in engineering structures [1,2]. Although UHPC exhibits strong resistance to cracking, its flexural (tensile)-to-compressive strength ratio at the cementitious matrix level is significantly lower than that of conventional concrete, rendering it still susceptible to matrix cracking under flexural (tensile) loading in practical applications [3]. In addition, UHPC typically undergoes pronounced early-age shrinkage. In combination with sustained service loads and environmental factors, it is difficult to completely avoid cracking of in-service UHPC members [4,5]. Nevertheless, UHPC generally contains an exceptionally high binder content and an extremely low water-to-binder ratio, which allows a considerable fraction of unhydrated particles to remain in the matrix over the long term, thereby providing a material basis for continued hydration and self-healing [6,7]. Therefore, enhancing the self-healing capacity of pre-damaged UHPC from the perspective of mix proportion design is of practical significance for extending service life, reducing maintenance frequency, and lowering costs [4,8].

*Article history: Received Dec 26, 2025; Accepted Apr 14, 2026*

Self-healing in cement-based materials is generally classified into autonomous self-healing and autogenous self-healing [6]. Autonomous self-healing relies on functional components such as shape-memory alloys [9], microcapsules [10], vascular networks [11], or microorganisms [12]. While its effectiveness is well documented, the associated cost and process complexity remain high, limiting large-scale implementation. By contrast, autogenous self-healing primarily depends on continued hydration and secondary reactions of cement and supplementary cementitious materials (SCMs), forming precipitates or gel phases within cracks to achieve crack filling. This approach is cost-effective, process-friendly, and more consistent with the intrinsic characteristics of UHPC [13–15]. In UHPC mixtures, the cement content often exceeds 700 kg/m$^3$ [16]. To reduce cost and carbon emissions, SCMs such as ground granulated blast furnace slag (GGBS) [17], silica fume (SF) [18], and fly ash [19] are widely used to partially replace cement. Moreover, studies have indicated that nanomaterials [20] and crystalline admixtures [21] can further improve self-healing performance. These materials possess pozzolanic activity and/or latent hydraulic reactivity to varying degrees, enabling sustained formation of reaction products over extended ages or reactions with hydration products, thereby endowing UHPC with a certain level of self-repair capacity even in the later stages of service.

Current research on autogenous self-healing of UHPC has largely focused on elucidating healing trends as a function of exposure conditions and crack characteristics. Xi et al. [22] explored the one-year self-healing process of pre-cracked UHPC in three different medium environments, noting that the self-healing level improved significantly with increasing exposure time, and the healing effect in tap water was superior to that in salt water and geothermal water. Yang et al. [23] examined the effects of superabsorbent polymer dosage and particle size on UHPC with preformed cracks of different widths, and compared healing performance under water curing, drying, and wet–dry cycles. Their results indicated that crack healing was most complete under water curing. Beglarigale et al. [24] discussed the crack self-healing mechanisms of UHPC from both macroscopic and microscopic perspectives, and suggested that compressive strength, crack closure, crack morphology analysis, permeability, total water absorption, and capillary water absorption can all be used to characterize the self-healing behavior of preloaded or pre-cracked UHPC. Regarding performance prediction, Xi et al. [25] adopted machine learning methods, selected crack width, exposure time and medium environment as input variables to establish a prediction model, and predicted the self-healing performance of UHPC under sustained tensile stress and corrosive environments over a 6-month period. The results indicated that exposure time and crack width were the dominant factors. Overall, while the environmental effects and characterization methods for self-healing concrete have been extensively discussed, systematic and quantitative investigations that specifically link mixture design to autogenous self-healing performance remain relatively limited.

Self-healing performance typically involves multidimensional responses, including crack closure, mechanical recovery, and enhanced densification. Without a unified evaluation framework, consistent comparison among different mixtures and reliable identification of parameter contributions are often difficult to achieve. As an objective weighting method for multi-index comprehensive evaluation based on data dispersion degree, the entropy weight method can determine the objective weights of multiple indices according to the variability of each index [26]. Accordingly, the entropy weight method has been widely applied in comprehensive assessments of concrete durability [27,28]. By contrast, most existing UHPC self-healing studies still interpret results primarily through individual indicators, and lack an objective integration of multi-indicator outcomes within a common evaluation system. This limitation hinders the establishment of more comparable quantitative rankings and optimization decisions for the overall self-healing capacity associated with different mixture-design parameters.

Response surface methodology (RSM) is a statistical modeling approach for multivariable problems. It obtains sample data through rational experimental design and employs a second-order regression model to describe the functional relationship between factors and responses, thereby enabling response prediction and parameter optimization [29]. In concrete mixture design studies, RSM can yield an interpretable, generalizable regression model with a relatively small number of experimental runs, substantially reducing experimental cost and workload [30,31]. Existing studies have demonstrated that RSM is well suited to UHPC mixture proportioning and performance optimization. For example, Ferdosian and Camões [32] used SF, ultrafine fly ash, and sand as variables to establish response relationships for UHPC workability and compressive strength. Wang et al. [33] applied RSM to analyze the effects of micro-coral sand and coral sand contents on the mechanical properties, durability, and autogenous shrinkage of UHPC. Mosaberpanah et al. [34] employed RSM to investigate the influences of nano-silica and waste glass powder on the mechanical performance, rheological behavior, and shrinkage of UHPC. However, no studies have yet been reported on the application of RSM to research on the self-healing performance of UHPC.

Accordingly, this study employed RSM for experimental design, with an emphasis on clarifying how

mixture proportions affect the autogenous self-healing performance of UHPC in a water environment. Crack closure at the surface, recovery of mechanical properties, and variations in ultrasonic pulse velocity (UPV) were adopted as the primary characterization methods to perform a multi-indicator evaluation of the self-healing process and recovery level of pre-damaged UHPC. On this basis, the entropy weight method was introduced to objectively assign weights to multiple indicators and to calculate an overall self-healing performance score. RSM regression equations were then established for compressive strength, flexural strength, and the comprehensive self-healing score. In addition, X-ray diffraction (XRD) was conducted to identify the phases of deposits formed in the crack region. The outcomes of this study are expected to provide mixture-design insights and quantitative support for the long-term safe service of UHPC components under complex exposure conditions.

## 2 Experimental program

### 2.1 Materials

The experiment employed P.I. 52.5 ordinary Portland cement supplied by Qingdao Shanshui Innovation Cement Co., Ltd., Class I fly ash from Laizhou Huadian Power Generation Co., Ltd., S95 GGBS from Gongyi Longze Water Treatment Materials Co., Ltd., and semi-densified SF produced by Chongqing Ximite Building Materials Co., Ltd. The chemical compositions of these cementitious materials are presented in Table 1. Copper-coated steel fibers were sourced from Hengshui Boge Metal Products Co., Ltd., with their basic properties listed in Table 2. The polycarboxylate-based high-performance superplasticizer (SP) used has a solid content of 13.51% and a water-reducing rate of 26%. The fine aggregate consists of quartz sand, which meets the requirements for continuous grading, and is a blend of four different particle sizes: 0.5–1.0, 0.4–0.6, 0.212–0.425, and 0.135–0.212 mm. The water used was laboratory tap water.

**Table 1** Chemical composition of cementitious materials (%)

| Oxide | Cement | Fly ash | GGBS | SF |
|---|---|---|---|---|
| $Al_2O_3$ | 4.2 | 41.56 | 17.70 | 0.550 |
| CaO | 63.63 | 4.16 | 34.00 | 0.528 |
| $Fe_2O_3$ | 3.89 | 4.93 | 1.03 | – |
| $K_2O$ | 0.38 | 0.67 | – | 0.282 |
| MgO | 2.15 | 0.42 | 6.01 | 0.496 |
| $Na_2O$ | 0.34 | 0.012 | – | 0.541 |
| $SO_3$ | 2.05 | 0.78 | 1.64 | 0.505 |
| $SiO_2$ | 17.37 | 43.45 | 34.50 | 96.72 |
| $TiO_2$ | 0.26 | 1.85 | – | – |

**Table 2** Basic properties of steel fibers

| Length (mm) | Diameter (mm) | Length-to-diameter ratio | Ultimate tensile strength (MPa) | Bending performance (%) | Relative density (g/cm$^3$) |
|---|---|---|---|---|---|
| 10 | 0.22 | 45.5 | ⩾ 2000 | ⩾ 90 | 7.8 |

### 2.2 Specimen preparation and curing

First, cement, fly ash, GGBS, SF, and quartz sand were added to a mixer and dry-mixed for 3 min to obtain a homogeneous dry blend. Subsequently, water and the high-performance SP were gradually introduced, and mixing was continued for 5 min to achieve a paste with adequate workability. Next, copper-coated steel fibers were slowly dispersed into the fresh mixture, followed by an additional 5 min of mixing to ensure uniform fiber distribution. The fresh UHPC was then rapidly cast into molds and vibrated on a vibration table for 30 s to eliminate entrapped air and voids. After casting, the molds were covered with plastic film and stored at room temperature for 24 h before demolding. Finally, the UHPC specimens were transferred to a standard curing room (20 ± 2 °C, relative humidity 95%) and cured for 28 d.

### 2.3 Mixture proportion design

In UHPC self-healing research, the most commonly adopted strategy is to incorporate SCMs [19,35]. In this study, fly ash content was fixed at 15% of the cement mass [36]. This level is widely used in practical mixture designs: it can improve later-age densification and durability while maintaining early-age strength development. Moreover, fly ash helps reduce hydration heat and improves the workability of the fresh paste [37]. GGBS and SF were incorporated as cement replacements within a system with a fixed total cementitious material content, rather than being added as extra materials while keeping the cement dosage constant. The total cementitious materials were kept constant at 1100 kg/m$^3$, and the mixing water content was fixed at 220 kg/m$^3$, yielding a water/binder ratio of 0.20. The dosage of SP was designed based on its mass ratio to cementitious materials, and controlled within the preset narrow range of 1.5%–2.5%. In this work, SP was mainly employed as an auxiliary regulating component. Its purpose was to ensure the castability and mixing uniformity of fresh UHPC in each group under consistent mixing process conditions, thereby guaranteeing the consistency and comparability of specimen forming conditions. Specifically, the fresh UHPC was deemed to meet the sample preparation requirements when it could be stably placed into molds without obvious segregation or bleeding, and exhibited uniform fiber dispersion.

In this study, the central composite design (CCD) of the RSM was adopted to carry out an experimental design with three factors and five levels. The three key influencing factors were specified as follows: GGBS dosage (by mass fraction of cement), SF dosage (by mass fraction of cement), and steel fiber volume dosage. Each factor was investigated at five coded levels ($-\alpha$, −1, 0, +1, $+\alpha$), with the specific values listed in Table 3. The schematic illustration of the three-factor CCD is presented in Fig. 1.

**Table 3** CCD input variables and their ranges

| Variable | Factor | Range of variable | | | | |
|---|---|---|---|---|---|---|
| | | −1.68 | −1 | 0 | +1 | +1.68 |
| GGBS (%) | *A* | 0 | 10 | 25 | 40 | 50 |
| SF (%) | *B* | 0 | 10 | 25 | 40 | 50 |
| Steel fiber (%) | *C* | 0.3 | 1 | 2 | 3 | 3.7 |

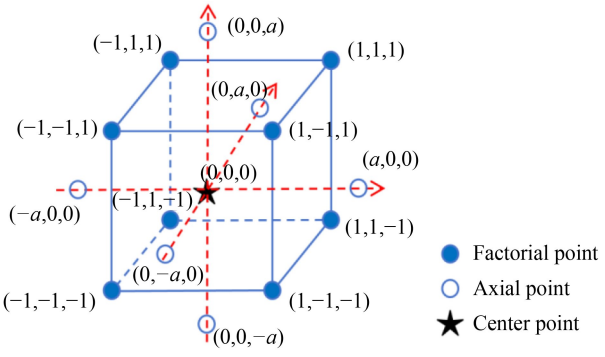



**Fig. 1** Schematic illustration of the CCD.

As depicted in Fig. 1, the CCD consisted of eight factorial points, six axial points, and one center point replicated six times. Accordingly, a total of 20 experimental runs were generated. The UHPC mixture proportions for each run are presented in Table 4. The response variables considered in this study included compressive strength, flexural strength, and the comprehensive self-healing performance score. Each response was fitted and predicted using the second-order polynomial regression model [36]:

$$y = \beta_0 + \sum \beta_i x_i + \sum \beta_{ii} x_i^2 + \sum \beta_{ij} x_i x_j, \quad (1)$$

where $y$ is the predicted response, $\beta_0$ is the intercept of the model, $\beta_i$ denotes the linear coefficient, $\beta_{ii}$ is the quadratic coefficient, $\beta_{ij}$ represents the interaction coefficient between variables, $x_i$ and $x_j$ are the independent variables.

## 2.4 Test methods

### 2.4.1 Compressive and flexural strength tests

Cubic specimens with dimensions of 40 mm × 40 mm × 40 mm were used for compressive strength tests, and prismatic specimens with dimensions of 40 mm × 40 mm × 160 mm were used for flexural strength tests. Mechanical property tests were carried out in accordance with the previous study [5]. The compressive tests were performed at a loading rate of 2.4 kN/s, while the flexural tests were performed at a loading rate of 50 N/s.

**Table 4** UHPC mixture proportions for the experimental design

| Group | Factor *A*, GGBS (%) | Factor *B*, SF (%) | Factor *C*, steel fiber (%) | SP (%) | Sand/ binder ratio | Water content (kg/m$^3$) | Water/ binder ratio |
|---|---|---|---|---|---|---|---|
| R1 | 10 | 10 | 3 | 2 | 0.9 | 220 | 0.2 |
| R2 | 0 | 25 | 2 | 2.5 | | | |
| R3 | 40 | 10 | 3 | 1.5 | | | |
| R4 | 25 | 25 | 2 | 2 | | | |
| R5 | 25 | 25 | 0.3 | 2 | | | |
| R6 | 40 | 10 | 1 | 1.5 | | | |
| R7 | 10 | 40 | 1 | 2.5 | | | |
| R8 | 50 | 25 | 2 | 2 | | | |
| R9 | 25 | 50 | 2 | 2.5 | | | |
| R10 | 25 | 25 | 3.7 | 2.5 | | | |
| R11 | 25 | 25 | 2 | 2 | | | |
| R12 | 25 | 25 | 2 | 2 | | | |
| R13 | 40 | 40 | 1 | 2.5 | | | |
| R14 | 25 | 25 | 2 | 2 | | | |
| R15 | 25 | 25 | 2 | 2 | | | |
| R16 | 25 | 0 | 2 | 1.5 | | | |
| R17 | 25 | 25 | 2 | 2 | | | |
| R18 | 10 | 10 | 1 | 2 | | | |
| R19 | 40 | 40 | 3 | 2.5 | | | |
| R20 | 10 | 40 | 3 | 2.5 | | | |

### 2.4.2 Pre-damage protocol and secondary curing environment

First, specimens from each mixture were loaded to failure to obtain the peak load, which was converted into the corresponding ultimate strength for that mixture and used as the basis for defining the pre-damage level. Subsequently, pre-damaged specimens were prepared [23,24]: for compressive specimens, loading was stopped and unloading was performed when the load reached 85% of the ultimate strength, so as to achieve controllable compressive pre-damage. For flexural specimens, loading was terminated when the load approached the peak strength (~100% of the ultimate strength), thus obtaining UHPC specimens with prefabricated cracks.

The secondary curing (self-healing) environment was set as full immersion in tap water. The pre-damaged specimens were continuously submerged in a water tank

until the specified healing age, in order to simulate the autogenous self-healing process under saturated conditions.

### 2.5 Ultrasonic pulse velocity recovery

Ultrasonic non-destructive testing was employed to evaluate changes in the internal integrity of UHPC specimens in the initial state, after pre-damage, and after the healing period. The instrument used was an HC-CS201 crack depth tester manufactured by Beijing Haichuang Gaoke Technology Co., Ltd. During testing, the transmitting and receiving transducers were positioned on opposite sides of the preformed crack, so that the ultrasonic wave generated at the transmitter propagated along a predefined path through the specimen and was recorded by the receiver. The UPV was then calculated to characterize the material condition.

### 2.6 X-ray diffraction

After 90 d of self-healing, surface deposits were gently scraped from the crack region along the crack direction, while minimizing the inclusion of matrix debris. The collected material was ground to achieve homogeneity and then sieved through a 200-mesh screen to reduce the influence of particle-size variation on diffraction intensity and peak shape. Phase identification was performed using a PANalytical X'Pert Powder X-ray diffractometer. The scan range was $2\theta$ = 5°–75°, with a total scan time of 30 min.

## 3 Results and discussion

### 3.1 Self-healing condition of crack surfaces

To track the self-healing process on crack surfaces, the crack morphology of specimens was photographed and recorded at 0 d after pre-damage and after 14, 28, and 90 d of autogenous healing under full immersion in water. Figure 2 presents a comparative visualization of four representative mixtures (R3, R16, R18, and R20) selected from the 20 groups because they exhibited relatively more pronounced crack-healing phenomena. The blue circles indicate the locations of the initial cracks, whereas the red circles highlight product deposition in the crack regions after the healing period.

As displayed in Fig. 2, the crack was through-going with sharp and well-defined edges at 0 d. After 14 d of healing, the crack remained clearly visible, with only a small amount of localized, spot-like deposits observed. At 28 d, light-gray or white strip-like deposits formed along the crack line, and the visible crack width decreased to a certain extent, yet sections with incomplete closure still existed. By 90 d, the deposit layer further thickened and became more continuously distributed, indicating that crack repair was promoted jointly by crack convergence and crack filling through product deposition. Under water-immersion conditions, these deposits are generally associated with two processes: 1) continued hydration of unhydrated binder particles and subsequent reactions of SCMs, producing low-crystallinity calcium silicate

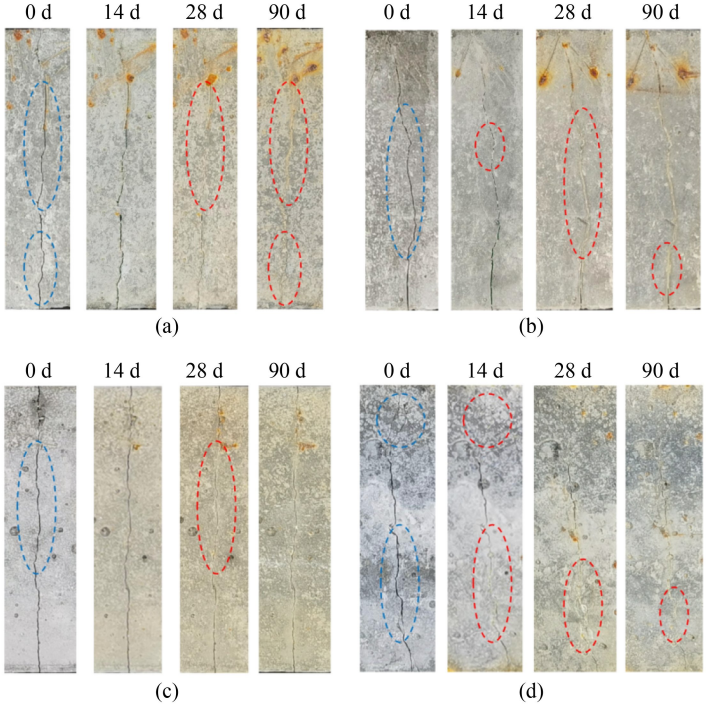



**Fig. 2** Evolution of crack width over time: (a) R3: $A$ = 40, $B$ = 10, $C$ = 3; (b) R16: $A$ = 25, $B$ = 0, $C$ = 2; (c) R18: $A$ = 10, $B$ = 10, $C$ = 1; (d) R20: $A$ = 10, $B$ = 40, $C$ = 3.

hydrate (C-S-H) that accumulates within the crack. 2) Dissolution and migration of $Ca(OH)_2$, followed by carbonation on the crack surface to form $CaCO_3$ adhering to the crack walls [18]. The synergy of these processes enhances the degree of filling and densification in the crack region. Similar hydration-regulated self-healing behavior has also been reported in mineral-based self-healing cementitious systems, in which sustained hydration promotes crack filling and structural regeneration [38].

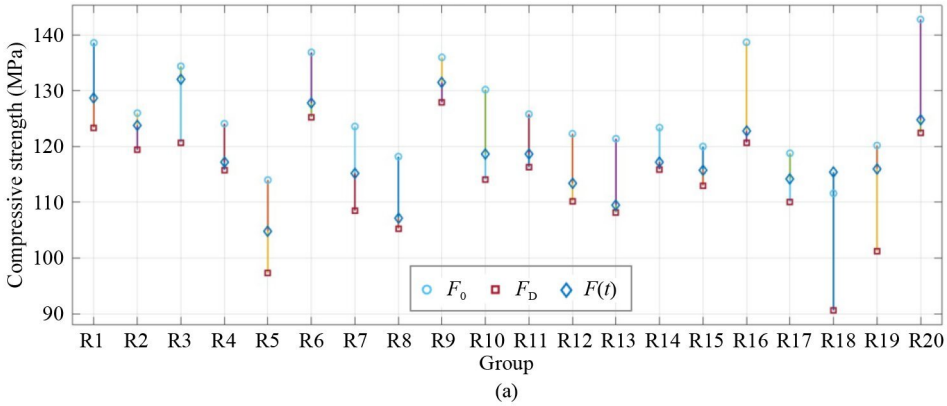
The self-healing effects of UHPC with different mix proportions exhibited significant differences. Specifically, relatively continuous crack filling bands were observed in Group R3 ($A$ = 40, $B$ = 10, $C$ = 3) and Group R20 ($A$ = 10, $B$ = 40, $C$ = 3) at the curing age of 28 d. The continuity of the filling bands was further improved at 90 d. This indicated that the high steel fiber volume fraction could effectively restrict the crack opening width, increase the re-contact probability of crack surfaces, and thereby provide a stable reaction space for the retention and accumulation of self-healing deposits. On this basis, the subsequent hydration reactions of SCMs could continuously supply products to the crack regions, promoting the evolution of deposits from scattered distribution to continuous filling. In contrast, although secondary hydration products were also detected in Group R16 ($A$ = 25, $B$ = 0, $C$ = 2) and Group R18 ($A$ = 10, $B$ = 10, $C$ = 1), the product distribution was relatively discrete and the crack closure degree was limited. This phenomenon was partly attributed to the weakened crack control and bridging effects caused by low fiber dosage. On the other hand, it also confirmed that the intrinsic self-healing of UHPC under water immersion conditions was more dependent on the synergistic effect between steel fibers and SCMs. When the crack opening width was large or the product supply was insufficient, it was difficult for the deposits to form continuous filling bands.

## 3.2 Strength recovery

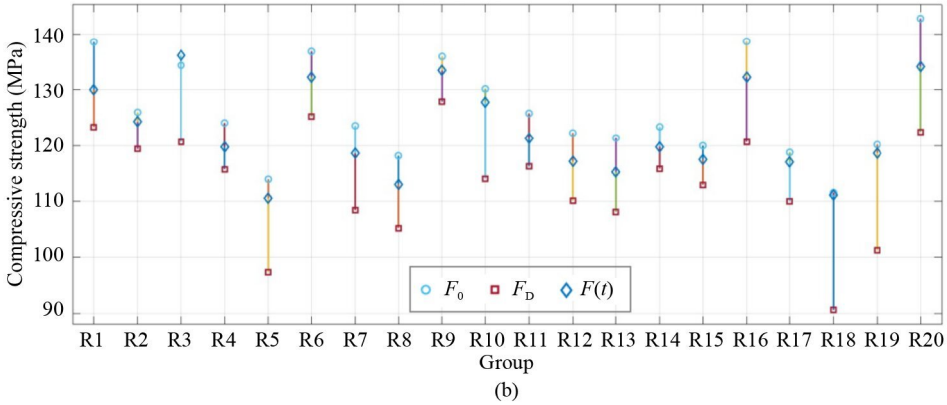
### 3.2.1 Compressive strength results

The recovery of compressive strength of pre-damaged specimens after immersion in water at different self-healing ages is presented in Fig. 3, where $F_0$ is the initial strength of the specimens, $F_D$ is the strength measured immediately after pre-damage, and $F(t)$ represents the compressive strength of the pre-damaged specimens after autogenous healing for $t$ d under water immersion conditions.

As displayed in Fig. 3, after pre-damage at approximately 85% of the peak load, the compressive strength of each mixture decreased from the initial value $F_0$ to $F_D$. Because this loading protocol did not generate visually detectable macrocracks, the strength reduction is more likely attributable to the progressive accumulation of microcracks and micro-damage in the matrix–aggregate interfacial transition zone (ITZ), around pores,



(a)



(b)

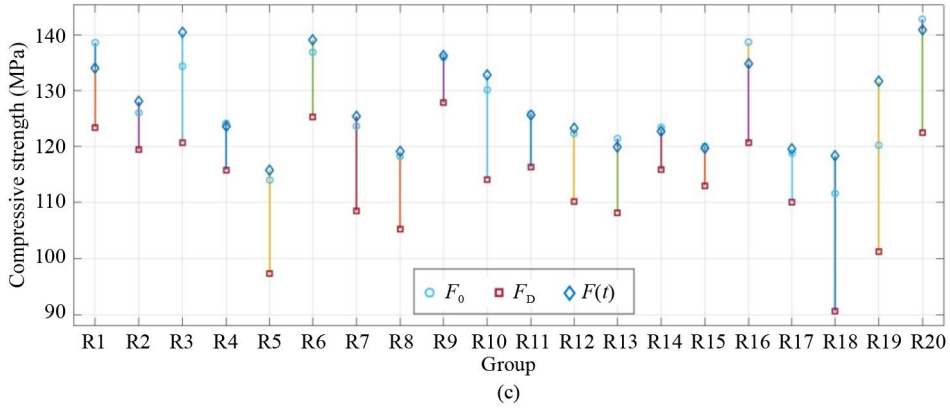



**Fig. 3** Compressive strength recovery of pre-damaged UHPC specimens after water immersion: (a) 14 d of self-healing; (b) 28 d of self-healing; (c) 90 d of self-healing.

and within the matrix during compression, which increases the material's sensitivity to defects. After subsequent curing under full water immersion, $F(t)$ generally increased with healing age and gradually approached $F_0$, demonstrating a clear time-dependent effect. This can be attributed to the sustained formation of secondary hydration products in the damaged zone, together with the normal long-term strength development of the material under prolonged immersion. In addition, mixtures with a higher steel-fiber volume fraction generally exhibited a smaller strength drop from $F_0$ to $F_D$ and a higher level of strength rebound in $F(t)$ (e.g., R3, R10, and R19). This indicates that fibers can restrain microcrack propagation and partially mitigate strain localization during compression, thereby reducing damage accumulation and enhancing subsequent self-healing performance. In contrast, low-fiber mixtures (e.g., R5: $C$ = 0.3) tended to show a larger damage-induced strength loss and a limited recovery between 14 and 28 d. Meanwhile, the SCMs exerted a more pronounced influence on mid- to late-age recovery: mixtures with higher GGBS and SF contents more readily achieved $F(t)$ values close to or exceeding $F_0$ at 28–90 d. This trend is consistent with the role of continued hydration and pozzolanic reactions in generating C-S-H and related products that fill micro-damaged regions and promote re-densification of the ITZ.

The compressive strength development of the undamaged control specimens under full water immersion at ages of 0, 14, 28, and 90 d is presented in Fig. 4. Overall, the strength of each group increased slowly with the extension of immersion time and tended to stabilize in the later stage. This phenomenon indicated that the water environment could continuously provide the moisture required for hydration reactions, promoting the gradual hydration of unhydrated cementitious materials, further facilitating the continuous densification of the matrix, and thus resulting in a certain degree of strength gain. In subsequent calculations of the compressive strength recovery rate of pre-damaged specimens, corrections will be made by incorporating the strength growth data of undamaged control specimens, so as to maximize the differentiation between the contributions from normal strength gain with age and self-healing recovery after damage.

### 3.2.2 Flexural strength results

The recovery of flexural strength of the pre-damaged

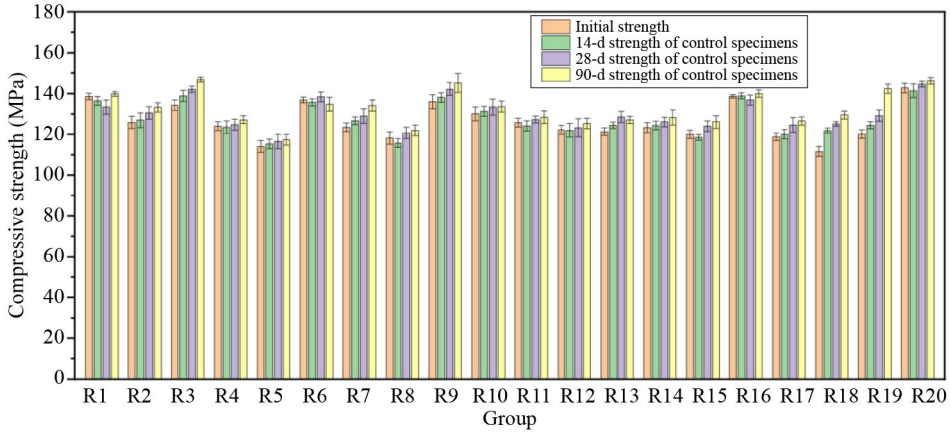



**Fig. 4** Compressive strength of undamaged control UHPC specimens after water immersion.

specimens after immersion in water at different self-healing ages is displayed in Fig. 5.

In contrast to the compressive specimens, where pre-damage was introduced without visible macrocracks, flexural pre-damage was dominated by crack formation. Consequently, the decrease from $F_0$ to $F_D$ is more sensitive to crack opening, crack path, and potential loss of fiber-bridging capacity. Overall, flexural strength exhibited a gradual recovery with increasing immersion time. It is worth noting that when the preformed crack opening was relatively large, effective recovery of flexural strength remained difficult even after 90 d of immersion. Comparison among mixtures indicates that the steel-fiber volume fraction played a dominant role in both the initial flexural strength and the recovery level. High-fiber mixtures (e.g., R3, R10, R19, and R20) generally exhibited higher $F_0$ values and stronger recovery capacity, and continued to show more evident improvement from 28 to 90 d. This confirms that fiber bridging increases the likelihood of re-contact between crack faces, thereby providing more favorable reaction space conditions for the retention and accumulation of healing products in the crack. Conversely, low-fiber mixtures (e.g., R5) showed relatively low initial flexural strength, a larger damage-induced reduction, and limited recovery. This behavior reflects insufficient restraint on

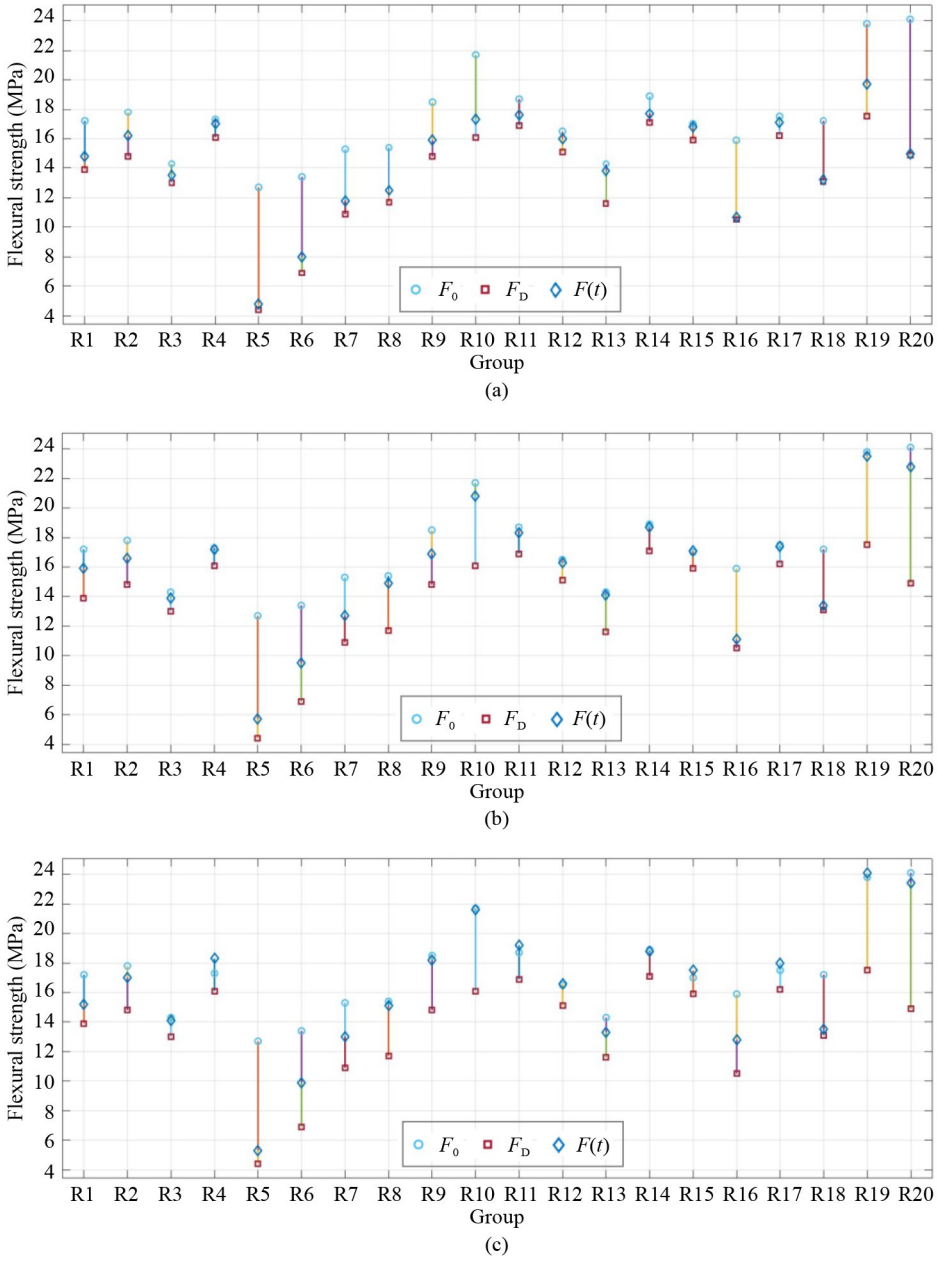



**Fig. 5** Flexural strength recovery of pre-damaged UHPC specimens after water immersion: (a) 14 d of self-healing; (b) 28 d of self-healing; (c) 90 d of self-healing.

crack opening, which prevents deposited products from forming load-bearing connections across the crack. Meanwhile, SCMs further enhanced mid- to late-age recovery. The groups with high dosages of SF or GGBS were more likely to exhibit a continuous upward trend in performance during the curing period of 28–90 d, which was consistent with the deposition of C-S-H gel generated by secondary hydration reactions, as well as the filling effect of $CaCO_3$ crystals to a certain extent. It can be concluded that there exists a synergistic effect between the supply of hydration products from SCMs and the crack control function of steel fibers, which jointly determine the recovery degree of UHPC flexural strength.

The flexural strength development of undamaged control specimens under full water immersion is presented in Fig. 6. These control results can be used to correct and benchmark the flexural recovery of pre-damaged specimens, thereby minimizing the influence of normal age-related strength gain induced by prolonged immersion and enabling an assessment that more closely reflects the self-healing contribution [24].

### 3.3 Ultrasonic testing

In the ultrasonic testing program, the initial UPV ($V_0$), the velocity measured immediately after pre-damage ($V_d$), and the velocity measured after 28 d of healing under full water immersion ($V_h$) were obtained for each group. The UPV variations of each group of specimens before and after healing are displayed in Fig. 7, where the orange segment represents the post-damage UPV level, the green segment denotes the UPV recovery attributable to 28 d of self-healing, and the gray segment indicates the residual loss relative to the initial state. All specimens exhibited a reduction in UPV after pre-damage, indicating that damage-induced cracks forced the ultrasonic wave to detour around discontinuities, effectively increasing the propagation path length and the arrival time, thereby reducing the apparent propagation velocity. After 28 d of healing, the UPV of most groups increased to varying degrees, suggesting that self-healing products formed within the cracks and near the crack walls, filled defects, and enhanced contact and connectivity across crack faces. This partially restored continuous transmission pathways, allowing wave propagation to become more direct and reducing the arrival time. Nevertheless, several mixtures retained a pronounced gray residual segment, indicating that within 28 d the repair was mainly associated with localized filling by healing products and was still insufficient to restore internal integrity to the initial level. In summary, UPV is sensitive to damage-induced discontinuities and healing-induced densification, and can serve as an effective non-destructive indicator for distinguishing self-healing performance among UHPC mixtures.

### 3.4 Development and results of the comprehensive self-healing performance evaluation

#### 3.4.1 Multi-indicator evaluation of ultra-high-performance concrete self-healing performance

In this study, the baseline recovery ratio (*BRR*), net self-healing ratio (*NSR*), and UPV–based self-healing score ($S_u$) were adopted to comprehensively evaluate the self-healing performance of UHPC. *BRR* and *NSR* are calculated for both compressive and flexural strengths, yielding $BRR_c$ and $NSR_c$ (compressive), as well as $BRR_f$ and $NSR_f$ (flexural). This evaluation method enables the quantitative evaluation of mechanical self-healing effects from two dimensions: the recovery level compared with the initial strength and the proportion of self-healing contribution in the total strength recovery. Compared with *BRR* and *NSR*, UPV provides a non-destructive characterization of crack closure and internal densification during healing, and thus complements the mechanical indicators by reflecting changes in internal integrity related to the recovery of effective material properties [39].

1) *BRR*. This indicator takes the initial strength of undamaged specimens as a unified reference, and is used to characterize the absolute strength level achieved by

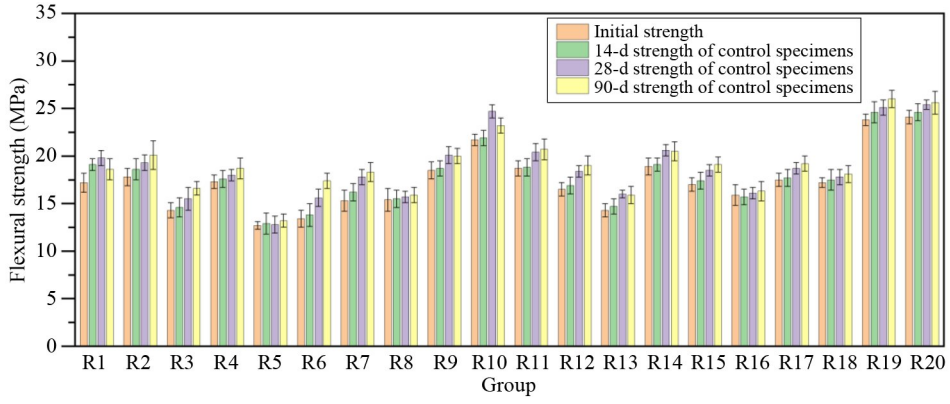



**Fig. 6** Flexural strength of undamaged control UHPC specimens after water immersion.

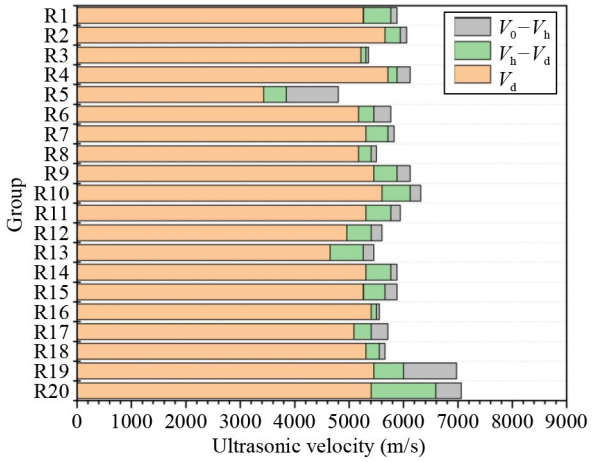



**Fig. 7** UPV changes before and after healing.

pre-damaged specimens after $t$ d of healing. Its advantages lie in its intuitiveness and convenience for horizontal comparison among specimens with different mix proportions. However, its calculated values also include the normal strength gain with age of the material itself under the water curing conditions, so it is more suitable for characterizing the final strength recovery level of specimens after healing.

$$BRR = \frac{f^{D}(t)}{f_0^{U}}, \tag{2}$$

where $f_0^{U}$ is the initial strength of the undamaged specimen, and $f^{D}(t)$ is the strength of the pre-damaged specimen after healing for $t$ d.

2) *NSR*. To minimize the interference caused by normal strength gain with age, *NSR* indicator takes the strength of undamaged control specimens at the same curing age as the reference benchmark [22]. It normalizes the strength recovery of pre-damaged specimens to the upper limit range of strength achievable under the same curing conditions, thereby enabling a more accurate characterization of the net contribution derived from the self-healing effect of pre-damaged specimens.

$$NSR = \frac{f^{D}(t) - f_0^{D}}{f^{U}(t) - f_0^{D}}, \tag{3}$$

where $f_0^{D}$ is the strength measured immediately after pre-damage, and $f^{U}(t)$ is the strength of the undamaged control specimen after healing for $t$ d.

3) UPV-based self-healing comprehensive score ($S_u$). This indicator simultaneously takes into account the absolute integrity after healing and the recovery amplitude relative to the damaged state, which can enhance the ability to distinguish the differences in self-healing performance of UHPC with different mix proportions. Among them, the completeness ratio is used to characterize the overall integrity of the healed specimens relative to the initial state; the improvement rate reflects the proportion of wave velocity loss caused by damage that is recovered through the self-healing process.

$$S_u = \alpha \times CR + \beta \times IR, \tag{4}$$

$$CR = \frac{V_h}{V_0}, \tag{5}$$

$$IR = \frac{V_h - V_d}{V_0 - V_d}, \tag{6}$$

where $CR$ is the completeness ratio, $IR$ is the improvement ratio. The weights were set as $\alpha = \beta = 0.5$, assigning equal importance to $CR$ and $IR$ to facilitate comprehensive comparison and ranking among different mixture designs. To further verify the robustness of the weighting scheme, a sensitivity analysis was performed by varying $\alpha$ from 0.3 to 0.7 (with $\beta = 1 - \alpha$). The results show that the overall ranking of all mixtures agrees closely with the equal-weight case ($\alpha$ = 0.5), with Spearman correlation coefficients above 0.98. The optimal mixture remains unchanged, and the maximum ranking variation is within 2 positions. This demonstrates that the conclusions are insensitive to small adjustments of $\alpha$ and $\beta$, confirming the rationality and reliability of the equal-weight assumption for the dataset in this study.

### 3.4.2 Multi-indicator results of ultra-high-performance concrete self-healing performance at 28 d

At the curing age of 28 d, the self-healing effect of UHPC is already well developed and the differences among mixtures can be clearly distinguished. Therefore, this study designates 28 d as the core evaluation age for self-healing performance, and conducts multi-indicator comparison, correlation analysis, comprehensive scoring via the entropy weight method, and response surface regression modeling accordingly. The multi-indicator test results at the 28 d healing age are summarized in Table 5.

The Pearson correlation coefficients (−1 to 1) among the UHPC self-healing indicators are presented in Fig. 8. The flexural indicators show high internal consistency, with the correlation coefficient between $BRR_f$ and $NSR_f$ reaching 0.66, indicating that mix proportions with more significant flexural strength recovery generally have higher net self-healing contributions; this aligns with the direct control of flexural failure by the crack opening, fiber bridging, intracrack filling mechanism, allowing mutual corroboration between the two indicators. In contrast, the compressive indicators exhibit weak internal correlation, between $BRR_c$ and $NSR_c$ coefficient is only at 0.15, which may stem from the fact that compressive pre-damage is dominated by internal micro-damage accumulation rather than obvious macro-cracks, resulting

**Table 5** Multi-indicator test results of UHPC self-healing performance

| Group | $BRR_f$ | $NSR_f$ | $BRR_c$ | $NSR_c$ | $IR$ | $CR$ | $S_u$ |
|---|---|---|---|---|---|---|---|
| R1 | 0.924 | 0.339 | 0.939 | 0.670 | 0.817 | 0.981 | 0.899 |
| R2 | 0.933 | 0.400 | 0.987 | 0.438 | 0.700 | 0.980 | 0.840 |
| R3 | 0.972 | 0.360 | 1.013 | 0.724 | 0.661 | 0.991 | 0.826 |
| R4 | 0.994 | 0.579 | 0.965 | 0.440 | 0.412 | 0.961 | 0.686 |
| R5 | 0.449 | 0.155 | 0.970 | 0.693 | 0.304 | 0.801 | 0.553 |
| R6 | 0.709 | 0.299 | 0.966 | 0.534 | 0.473 | 0.945 | 0.709 |
| R7 | 0.830 | 0.261 | 0.960 | 0.490 | 0.785 | 0.981 | 0.883 |
| R8 | 0.968 | 0.800 | 0.957 | 0.503 | 0.701 | 0.982 | 0.842 |
| R9 | 0.914 | 0.396 | 0.982 | 0.392 | 0.641 | 0.961 | 0.801 |
| R10 | 0.959 | 0.547 | 0.982 | 0.710 | 0.727 | 0.969 | 0.848 |
| R11 | 0.979 | 0.400 | 0.964 | 0.450 | 0.728 | 0.971 | 0.850 |
| R12 | 0.988 | 0.364 | 0.958 | 0.534 | 0.689 | 0.964 | 0.826 |
| R13 | 0.986 | 0.568 | 0.950 | 0.346 | 0.762 | 0.965 | 0.863 |
| R14 | 0.989 | 0.457 | 0.971 | 0.379 | 0.802 | 0.981 | 0.892 |
| R15 | 1.006 | 0.462 | 0.979 | 0.405 | 0.642 | 0.962 | 0.802 |
| R16 | 0.698 | 0.107 | 0.954 | 0.720 | 0.661 | 0.991 | 0.826 |
| R17 | 0.994 | 0.480 | 0.986 | 0.476 | 0.509 | 0.946 | 0.728 |
| R18 | 0.779 | 0.064 | 0.996 | 0.594 | 0.701 | 0.981 | 0.841 |
| R19 | 0.987 | 0.789 | 0.988 | 0.623 | 0.358 | 0.860 | 0.609 |
| R20 | 0.946 | 0.752 | 0.940 | 0.527 | 0.719 | 0.934 | 0.826 |

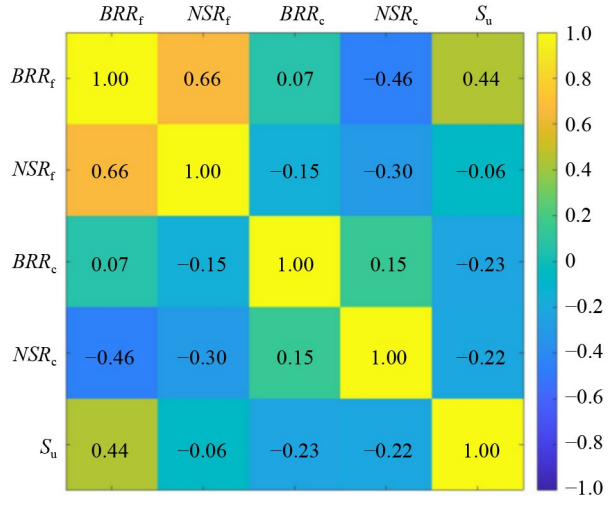



**Fig. 8** Heatmap of the correlation matrix among performance indicators.

in certain mixes indicating high $BRR_c$ but unremarkable $NSR_c$. Flexural and compressive indicators do not always vary synchronously, reflecting their distinct self-healing mechanisms: flexural strength recovery relies on crack surface reconnection and trans-crack load-bearing capacity reconstruction, while compressive strength recovery is governed by micro-damage degree, pore structure evolution and matrix densification level. The UPV-based comprehensive healing score ($S_u$) has moderate to weak correlations with all mechanical indicators, implying that enhanced internal densification and defect connectivity cannot be fully converted into strength recovery within 28 d of curing. In summary, the five indicators are interrelated yet independent; reliance on a single indicator tends to cause one-sided conclusions, thus necessitating a multi-indicator integrated evaluation and comprehensive scoring approach.

Figure 9 presents the five indicators used for comprehensive evaluation, as summarized in Table 5. Figure 9(a) is arranged in the order of original groups, which clearly reveals that the mix proportions vary significantly across different indicators, with high values not appearing synchronously in each indicator column. This demonstrates that the self-healing performance of UHPC features distinct multi-dimensional characteristics. By contrast, Fig. 9(b) conducts clustering and reordering for both groups and indicators simultaneously, based on data similarity without assigning any weights. Analysis of the bright-color distribution patterns of each group indicates that the mixes with concurrently higher $BRR_f$ and $S_u$ values generally contain a steel fiber volume fraction of 2%–3% along with a certain amount of GGBS and SF. This finding verifies that the synergistic effect between fiber-induced crack control and bridging, as well as the sustained product supply from later-stage SCMs reactions, facilitates the synchronous recovery of crack closure and overall structural integrity. On the contrary,

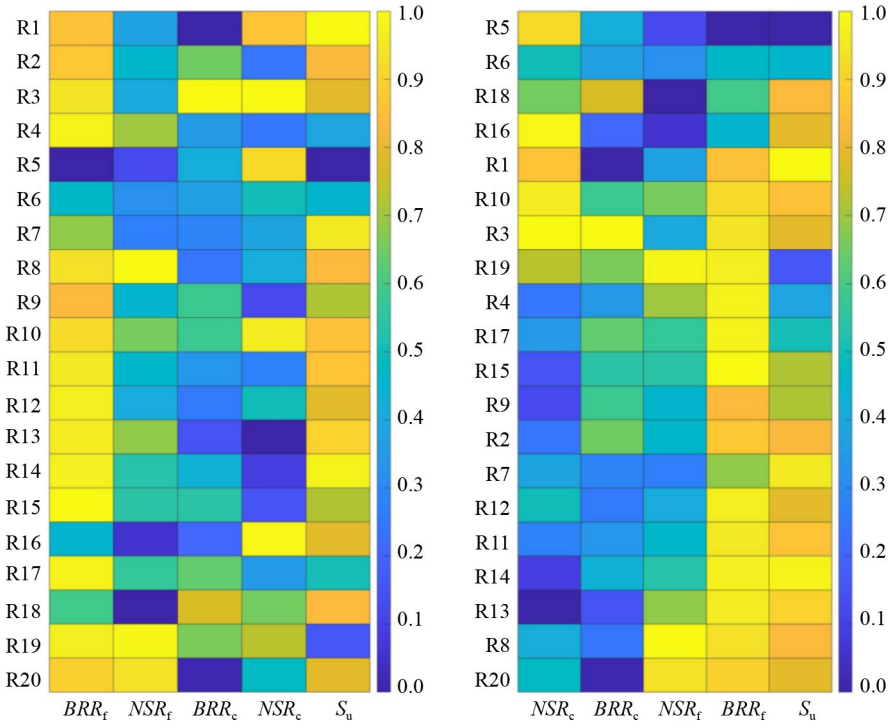



**Fig. 9** Heatmaps of self-healing performance indicators for UHPC mixtures: (a) unclustered; (b) cluster analysis.

groups with higher $NSR_c$ or $BRR_c$ but lower $NSR_f$ values are mostly characterized by insufficient fiber content or a single-component SCM system, exhibiting remarkable compressive property recovery driven by matrix densification yet inadequate restoration of trans-crack load-bearing capacity, which results in unsatisfactory net flexural strength recovery. Therefore, the combination of heatmap clustering analysis and subsequent comprehensive scoring enables a more holistic characterization of the self-healing performance of UHPC.

### 3.4.3 Comprehensive self-healing performance score based on the entropy weight method

As can be seen from the heatmap, the indicators do not always vary in the same direction, and it is difficult to draw stable ranking conclusions based on a single indicator. Therefore, it is necessary to introduce a comprehensive evaluation method capable of objectively determining indicator weights. In this study, the entropy weight method was adopted to assign weights to each indicator and calculate the comprehensive score, so as to achieve unified ranking and optimization of the mix proportion groups. The evaluation indicators include both strength-recovery indicators (*BRR* and *NSR*) and the UPV-based indicator ($S_u$), which reflect macroscopic load-bearing recovery as well as surface and internal improvement, respectively, thereby improving the robustness and interpretability of the conclusions. The calculation procedure of the entropy weight method is summarized as follows [26].

1) Data normalization. Because the indicators differ in units and value ranges, the original data must first be converted into dimensionless form and mapped to the interval of [0,1], so as to ensure that all indicators are comparable on the same scale.

$$Z_{ij} = \frac{X_{ij} - \min X_j}{\max X_j - \min X_j}, \tag{7}$$

where $X_{ij}$ is the original value of the $j$th indicator for the $i$th sample, and max $X_j$ and min $X_j$ denote the maximum and minimum values of the $j$th indicator among all experimental mixtures, respectively.

2) Positive translation. After standardizing all evaluation indicators, a uniform positive shift of 0.01 is applied to all standardized values in this study, so as to avoid numerical instability caused by ln0 or zero probabilities during the probabilistic conversion and entropy calculation.

$$Z'_{ij} = Z_{ij} + 0.01. \tag{8}$$

3) Proportion transformation. In the entropy weight method, the normalized data are further converted into the proportion of each group under the same indicator, so as to reflect the distribution characteristics of the indicator across different groups.

$$p_{ij} = Z'_{ij} / \sum_i Z'_{ij}. \tag{9}$$

4) Entropy calculation. The information entropy of the $j$th indicator is calculated as

$$e_j = -k\sum_i p_{ij}\ln p_{ij}, \tag{10}$$

$$k = 1/\ln n, \tag{11}$$

where $n$ is the number of samples, and the constant $k$ is introduced to ensure that $0 \leqslant e_j \leqslant 1$.

5) Redundancy calculation. A greater $d_j$ indicates that the corresponding indicator has a stronger capability to discriminate among mixtures.

$$d_j = 1 - e_j. \tag{12}$$

6) Determination of indicator weights. The weights are automatically determined by the dispersion of each indicator across the samples, rather than by subjective judgment. This effectively reduces potential bias introduced by manual weighting.

$$w_j = d_j/\sum d_j. \tag{13}$$

The weights of different self-healing performance indicators are presented in Table 6. As displayed in Table 6, the combined weight of $NSR_c$ and $NSR_f$ exceeds 50%, indicating that in the comprehensive evaluation of this study, $NSR$ indicators have a stronger ability to distinguish between different mix proportion designs and can provide more valid information, thus playing a more crucial role in the comprehensive evaluation. With undamaged control specimens as the reference, $NSR$ reduces the influence of strength growth during normal curing periods, and it focuses more on reflecting the net recovery contribution of pre-damaged specimens during the healing process, thereby better reflecting the essential differences in the intrinsic self-healing capacity of the material.

7) Calculation of the comprehensive self-healing score. The normalized indicators were multiplied by their corresponding weights and summed to obtain the comprehensive score $S_i(t)$ for mixture $i$ at healing age $t$.

$$S_i(t) = \sum_j w_j Z_{ij}. \tag{14}$$

The comprehensive scores of UHPC self-healing performance at the curing age of 28 d are presented in Table 7. The results show that the scores range from 0.40 to 0.83, with significant differences among groups. Among them, groups R3, R10, and R19 achieve higher scores. These groups all adopt a relatively high steel fiber volume fraction combined with a certain proportion of GGBS and SF, suggesting a clear advantage in overall self-healing performance. In contrast, groups with low steel fiber volume fractions (e.g., R13, R5, and R6) yielded relatively low scores, indicating that crack closure and multi-indicator recovery were collectively constrained.

**Table 6** Weights of different self-healing performance indicators

| Indicator | $BRR_f$ | $NSR_f$ | $BRR_c$ | $NSR_c$ | $S_u$ |
|---|---|---|---|---|---|
| $w_j$ | 0.094 | 0.229 | 0.254 | 0.294 | 0.129 |

## 3.5 Response surface analysis

### 3.5.1 Analysis of variance (ANOVA) and model validation

A response surface regression model was adopted to fit the compressive strength, flexural strength, and comprehensive self-healing performance score. The results of model statistical tests and residual diagnosis demonstrated that all three models exhibited good validity and predictive capability. The ANOVA results for the three models are presented in Tables 8–10. All models are statistically significant ($p < 0.0001$), demonstrating that GGBS, SF, and steel fibers, together with their quadratic and interaction terms, can effectively describe the variation patterns of the responses. Meanwhile, the lack-of-fit terms are not significant, indicating that within the experimental error, the quadratic models agree well with the measured data and

**Table 7** Comprehensive self-healing score of UHPC at 28 d and indicator weights

| Group | $BRR_f$-$w$ | $NSR_f$-$w$ | $BRR_c$-$w$ | $NSR_c$-$w$ | $S_u$-$w$ | $S_i$ |
|---|---|---|---|---|---|---|
| R1 | 0.080 | 0.086 | 0.000 | 0.252 | 0.129 | 0.547 |
| R2 | 0.082 | 0.105 | 0.162 | 0.071 | 0.107 | 0.527 |
| R3 | 0.088 | 0.092 | 0.254 | 0.294 | 0.102 | 0.830 |
| R4 | 0.092 | 0.160 | 0.091 | 0.072 | 0.050 | 0.465 |
| R5 | 0.000 | 0.028 | 0.107 | 0.269 | 0.000 | 0.405 |
| R6 | 0.044 | 0.073 | 0.094 | 0.146 | 0.058 | 0.416 |
| R7 | 0.064 | 0.061 | 0.071 | 0.112 | 0.123 | 0.432 |
| R8 | 0.088 | 0.229 | 0.062 | 0.122 | 0.108 | 0.608 |
| R9 | 0.078 | 0.103 | 0.146 | 0.035 | 0.093 | 0.455 |
| R10 | 0.086 | 0.150 | 0.146 | 0.283 | 0.110 | 0.775 |
| R11 | 0.089 | 0.105 | 0.087 | 0.081 | 0.111 | 0.473 |
| R12 | 0.091 | 0.093 | 0.067 | 0.146 | 0.102 | 0.499 |
| R13 | 0.091 | 0.157 | 0.038 | 0.000 | 0.116 | 0.401 |
| R14 | 0.091 | 0.122 | 0.109 | 0.025 | 0.127 | 0.474 |
| R15 | 0.094 | 0.124 | 0.137 | 0.046 | 0.093 | 0.494 |
| R16 | 0.042 | 0.013 | 0.052 | 0.291 | 0.102 | 0.500 |
| R17 | 0.092 | 0.129 | 0.160 | 0.101 | 0.065 | 0.547 |
| R18 | 0.056 | 0.000 | 0.196 | 0.192 | 0.108 | 0.552 |
| R19 | 0.091 | 0.226 | 0.166 | 0.215 | 0.021 | 0.719 |
| R20 | 0.084 | 0.214 | 0.004 | 0.141 | 0.102 | 0.545 |

**Table 8** ANOVA results for the compressive strength model

| Source | Sum of squares | Mean square | *F*-value | *p*-value | Remarks |
|---|---|---|---|---|---|
| Model | 1422.25 | 237.04 | 44.47 | < 0.0001 | significant |
| Lack of fit | 35.12 | 4.39 | 0.64 | 0.7252 | not significant |

**Table 9** ANOVA results for the flexural strength model

| Source | Sum of squares | Mean square | *F*-value | *p*-value | Remarks |
|---|---|---|---|---|---|
| Model | 167.21 | 33.44 | 40.85 | < 0.0001 | significant |
| Lack of fit | 6.91 | 0.77 | 0.84 | 0.6131 | not significant |

**Table 10** ANOVA results for the comprehensive self-healing score model

| Source | Sum of squares | Mean square | *F*-value | *p*-value | Remarks |
|---|---|---|---|---|---|
| Model | 0.25 | 0.042 | 45.07 | < 0.0001 | significant |
| Lack of fit | 0.007718 | 0.0009647 | 1.06 | 0.4955 | not significant |

no evident systematic bias is observed. The goodness-of-fit statistics for the three models are listed in Table 11. Both $R^2$ and adjusted $R^2$ (Adj-$R^2$) exceed 0.90, suggesting that more than 90% of the response variability is explained by the models and that high explanatory power is retained even after accounting for the number of predictors. The predicted $R^2$ (Pred-$R^2$) values are close to the Adj-$R^2$ values, with differences well below 0.20, indicating good predictive consistency within the design space [40]. In addition, the adequate precision values are substantially higher than 4, which is generally considered acceptable, indicating a high signal-to-noise ratio and the ability to distinguish response differences caused by factor variations [36].

Further validation is performed using the diagnostic plots in Figs. 10–12: the residuals are approximately distributed along a straight line in the normal probability plot, indicating that the residuals conform to an approximate normal distribution. The residual-predicted value scatter points are randomly distributed around zero without obvious funnel-shaped patterns or systematic trends, which verifies the homogeneity of variance and rationality of the model setup. No drift with respect to the experimental run order is observed in the residual-run order plot, indicating good independence of the residuals. The scatter points of predicted values and measured values are generally close to the 45° reference line, indicating that the model has high fitting and prediction accuracy. In summary, the three response surface models exhibit sufficient fitting, insignificant lack-of-fit, and residuals that satisfy the regression assumptions. They possess high explanatory power and prediction accuracy, and thus can be applied to subsequent factor effect analysis, response surface visualization, and mix proportion optimization.

**Table 11** Model validation statistics for the three response models

| Response | Compressive strength | Flexural strength | Comprehensive self-healing score |
|---|---|---|---|
| $R^2$ | 0.9535 | 0.9358 | 0.9541 |
| Adj-$R^2$ | 0.9321 | 0.9129 | 0.933 |
| Pred-$R^2$ | 0.8801 | 0.8708 | 0.8942 |
| Standard deviation | 2.31 | 0.9 | 0.031 |
| Adequate precision | 23.032 | 21.389 | 22.95 |

### 3.5.2 Response surfaces for compressive strength

The regression model for compressive strength in terms of coded variables is expressed as follows:

$$\text{Compressive strength}_{28-\text{d}}\ (\text{MPa}) = +122.55 - 1.23 \times A - 1.33 \times B + 5.08 \times C - 5.74 \times AB - 6.24 \times AC + 5.60 \times B^2, \quad (15)$$

where $A$, $B$, and $C$ denote the GGBS, SF and steel-fiber content, respectively.

Figure 13 presents the response surface plots of compressive strength. According to the regression equation, the contribution of steel fibers to compressive strength is positive and relatively large (the coefficient of $C$ is +5.08), which is consistent with the trend in Fig. 13 showing that the overall strength level increases as the fiber content rises from 1% to 2% and 3%. During the compression process, fibers can delay the initiation and propagation of microcracks, improve the stability of the failure process through fiber bridging, energy dissipation via fiber pull-out, and stress redistribution, and thus enhance the peak load-bearing capacity [41]. In contrast, the linear term of GGBS is negative, and the interaction terms $AB$ and $AC$ are also negative, indicating that within the investigated range, increasing GGBS tends to diminish the benefits provided by SF or steel fibers. A high GGBS content reduces the clinker content and may retard reaction kinetics, leading to insufficient early-age matrix strength and a weaker interfacial load-transfer basis [42]. By comparison, SF typically refines the pore structure via micro-filling and pozzolanic reactions, improves the ITZ, and enhances matrix densification,

which is beneficial for compressive strength and for mobilizing the reinforcing effects of steel fibers [18,43].

Converted to the practical dosage range, within the experimental design domain of this study, relatively high

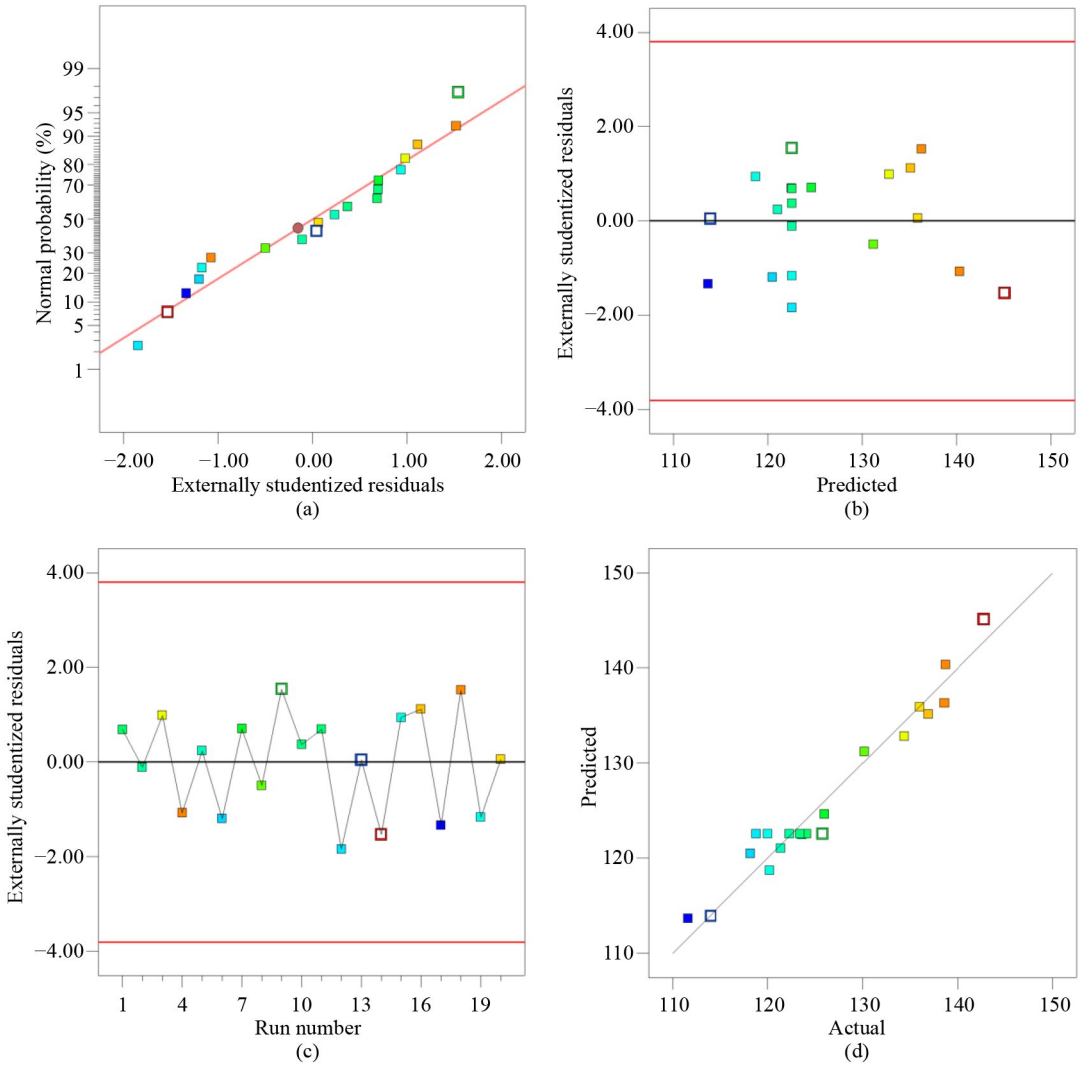
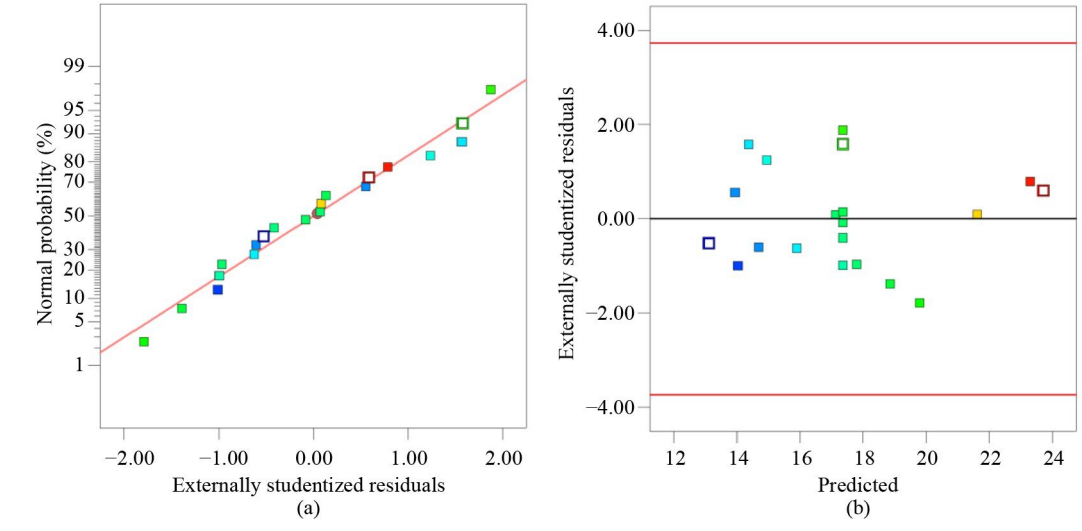



**Fig. 10** Diagnostic plots for the compressive strength model: (a) normal plot of residuals; (b) residuals vs. predicted; (c) residuals vs. run; (d) predicted vs. actual.



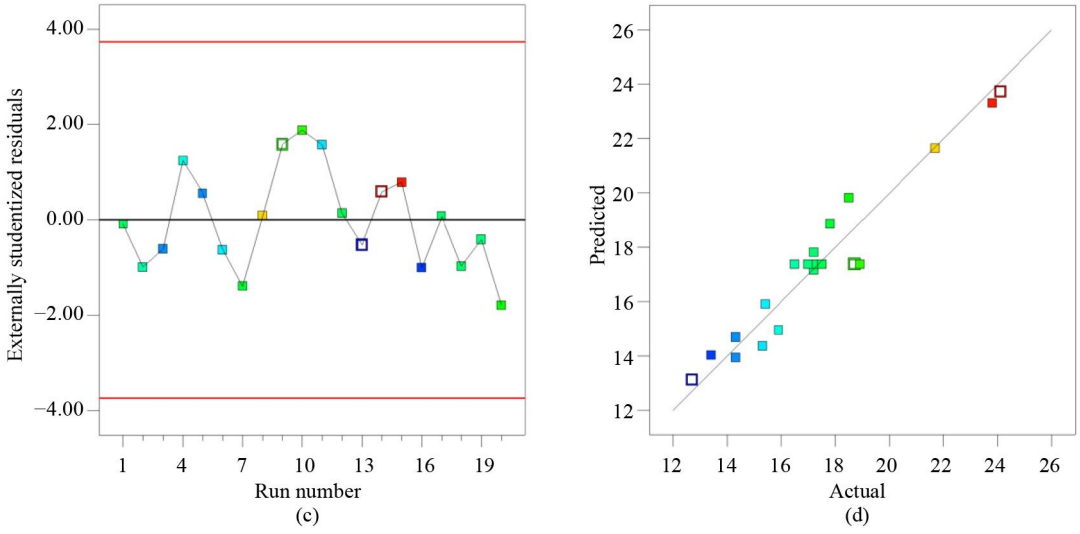



**Fig. 11** Diagnostic plots for the flexural strength model: (a) normal plot of residuals; (b) residuals vs. predicted; (c) residuals vs. run; (d) predicted vs. actual.

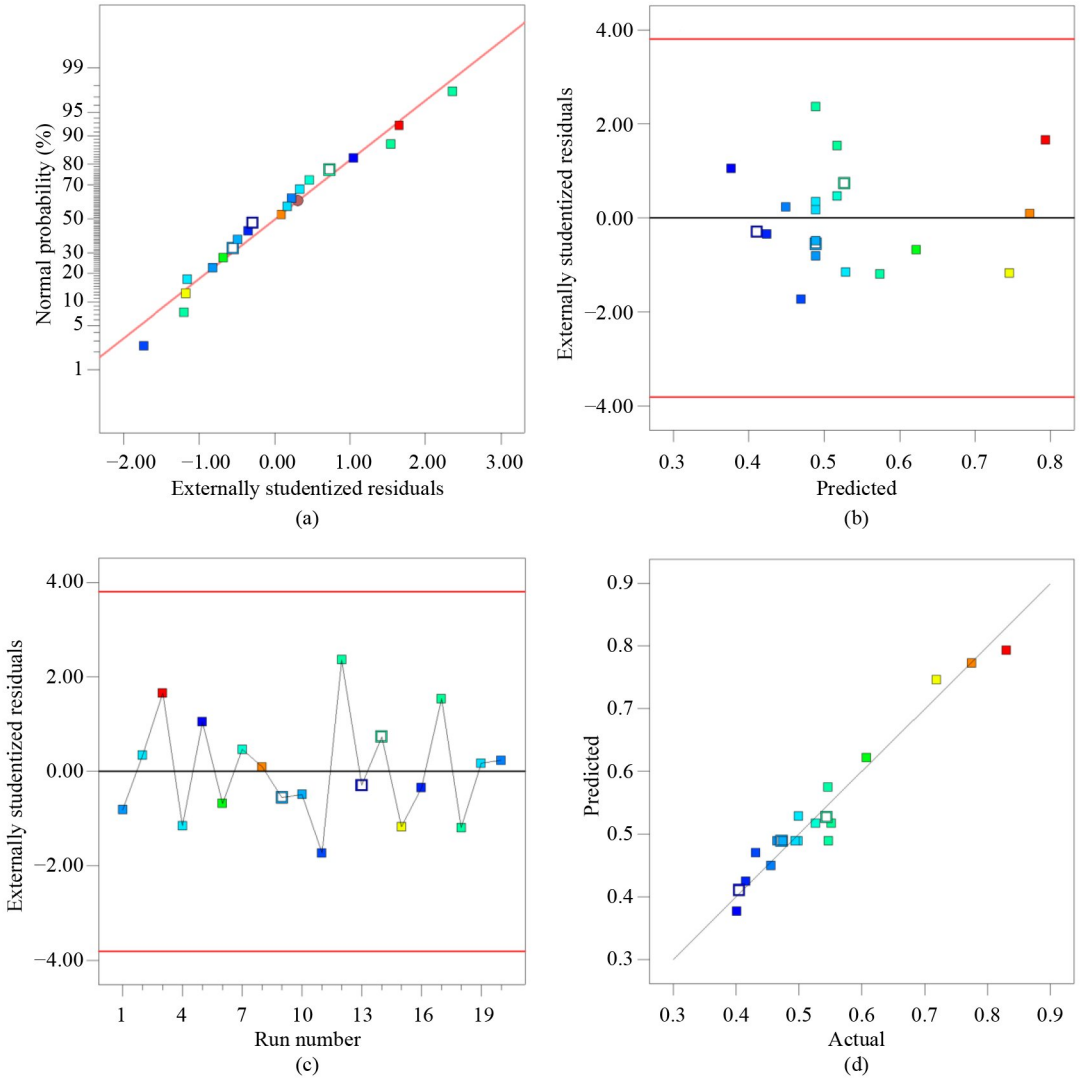



**Fig. 12** Diagnostic plots for the comprehensive self-healing score model: (a) normal plot of residuals; (b) residuals vs. predicted; (c) residuals vs. run; (d) predicted vs. actual.

compressive strength is mainly concentrated in the mix proportion interval featuring high fiber content, high SF content, and low GGBS content. A local concave feature appears in the lower-right area of Fig. 13(c), with the contour lines exhibiting bending. This indicates that when the GGBS dosage is increased to a medium or high level (approximately ⩾ 25%), affected by the antagonistic effect between GGBS and fibers (interaction term *AC*), the compressive strength does not necessarily increase synchronously even if the fiber content remains high.

### 3.5.3 Response surfaces for flexural strength

The regression model for the 28-d flexural strength in terms of coded variables is expressed as follows:

$$\text{Flexural strength}_{28-\text{d}}(\text{MPa}) = +17.38 - 0.89\times A + 1.46\times B + 2.50\times \text{C} + 0.68\times AB + 2.18\times BC, \quad (16)$$

where *A*, *B*, and *C* denote the GGBS, SF and steel-fiber content, respectively.

Figure 14 presents the response surface results for flexural strength. As indicated by the regression equation, flexural strength is still dominated by steel fibers (coefficient of *C*: +2.50). SF shows a pronounced positive effect (coefficient of *B*: +1.46), and a strong positive synergy exists between SF and fibers (coefficient of *BC*: +2.18). The peak flexural load is primarily governed by the load-transfer capacity across the main crack, and fiber bridging is the key mechanism controlling crack-bridging load transfer and stable crack propagation [41]. SF improves matrix densification and the fiber-matrix interfacial quality through micro-filling and pozzolanic reactions, thereby enhancing interfacial bonding and frictional resistance. As a result, the fiber-bridging effect can be more effectively translated into an increase in flexural load-bearing capacity. A comparison between Figs. 14(b) and 14(c) further indicates that, under high-fiber slices, the response surface exhibits a steeper gradient along the SF direction.

Within the practical dosage range, the optimal region for the flexural strength is more inclined toward the mix

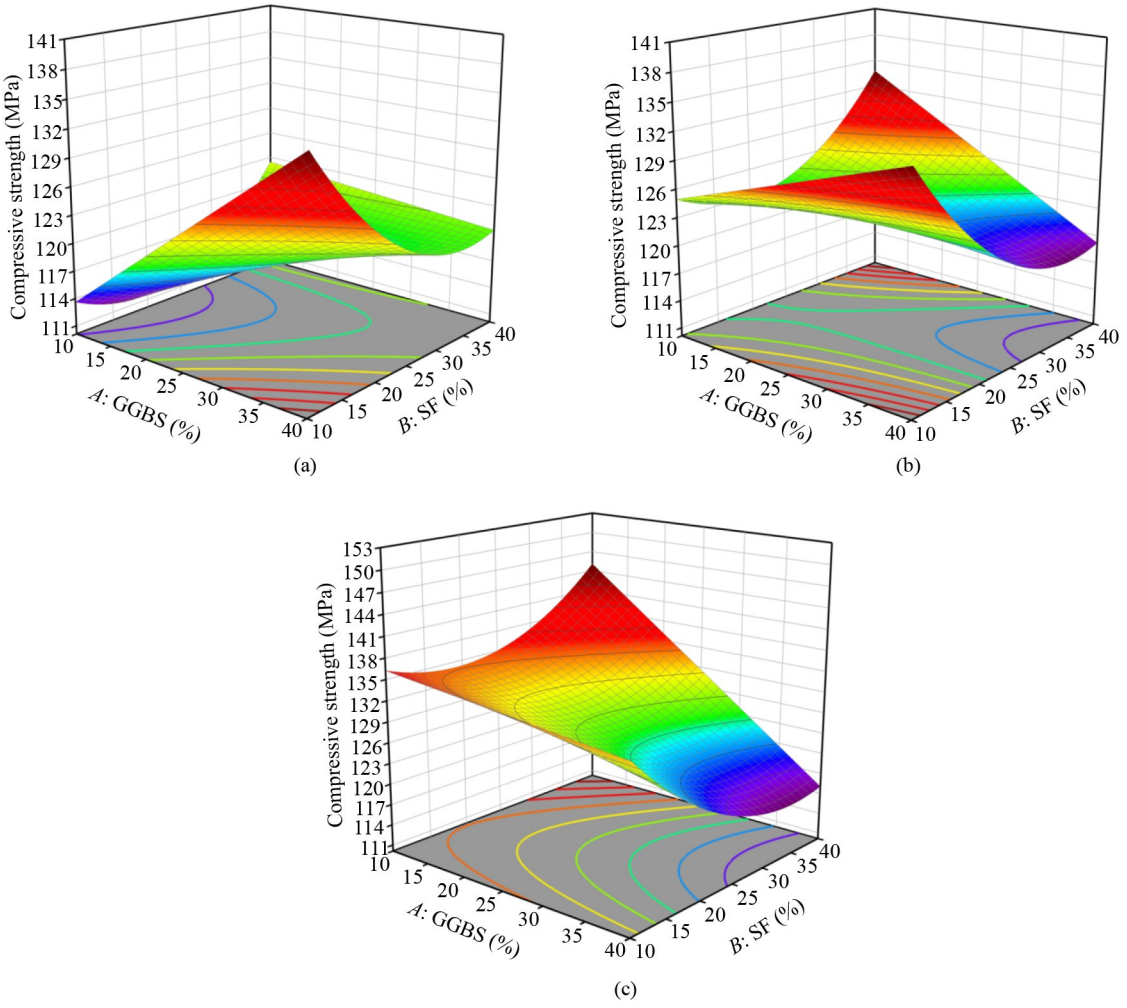



**Fig. 13** Compressive strength versus GGBS and SF at 1%, 2%, and 3% steel fiber: (a) at 1% steel fiber volume fraction; (b) at 2% steel fiber volume fraction; (c) at 3% steel fiber volume fraction.

proportion combination featuring high fiber content and high SF content. Although the linear term of GGBS (Factor $A$) exhibits a negative effect, its adverse impact can be offset to a certain extent under the condition of high SF content (with the interaction term $AB > 0$). Therefore, a medium-to-high dosage of GGBS can be adopted to synergistically optimize the particle gradation and interfacial densification of the system [42]. From the surface topography depicted in Fig. 14, the trend along GGBS direction shifts from decreasing to increasing in the region with high SF content.

### 3.5.4 Response surfaces for the comprehensive self-healing score

The regression model for the comprehensive self-healing score in terms of coded variables is expressed as follows:

$$\text{Comprehensive self}-\text{healing score} = +0.49 + 0.031A - 0.024B + 0.11C + 0.078AC + 0.029A^2 + 0.036C^2, \quad (17)$$

where $A$, $B$, and $C$ denote the GGBS, SF and steel-fiber content, respectively.

Figure 15 illustrates the response surfaces of the comprehensive self-healing score. The linear term $C$ and the quadratic term $C^2$ are both positive, suggesting that, under the evaluation framework adopted in this study, increasing fiber content is beneficial for enhancing overall self-healing performance. Fibers can restrain crack opening and crack-face sliding, increase the probability of crack re-contact, and improve the retention and accumulation efficiency of healing products in the crack region. Moreover, the positive $AC$ interaction indicates a synergistic effect between GGBS and steel fibers. Fiber-based crack control and bridging provide more stable geometric conditions for self-healing, whereas GGBS contributes through later-age secondary hydration, enabling sustained product formation and microstructural densification. Their combined action results in a more robust increase in the comprehensive score. In contrast, the linear term of SF exhibits a weakly negative effect (with a small coefficient magnitude),

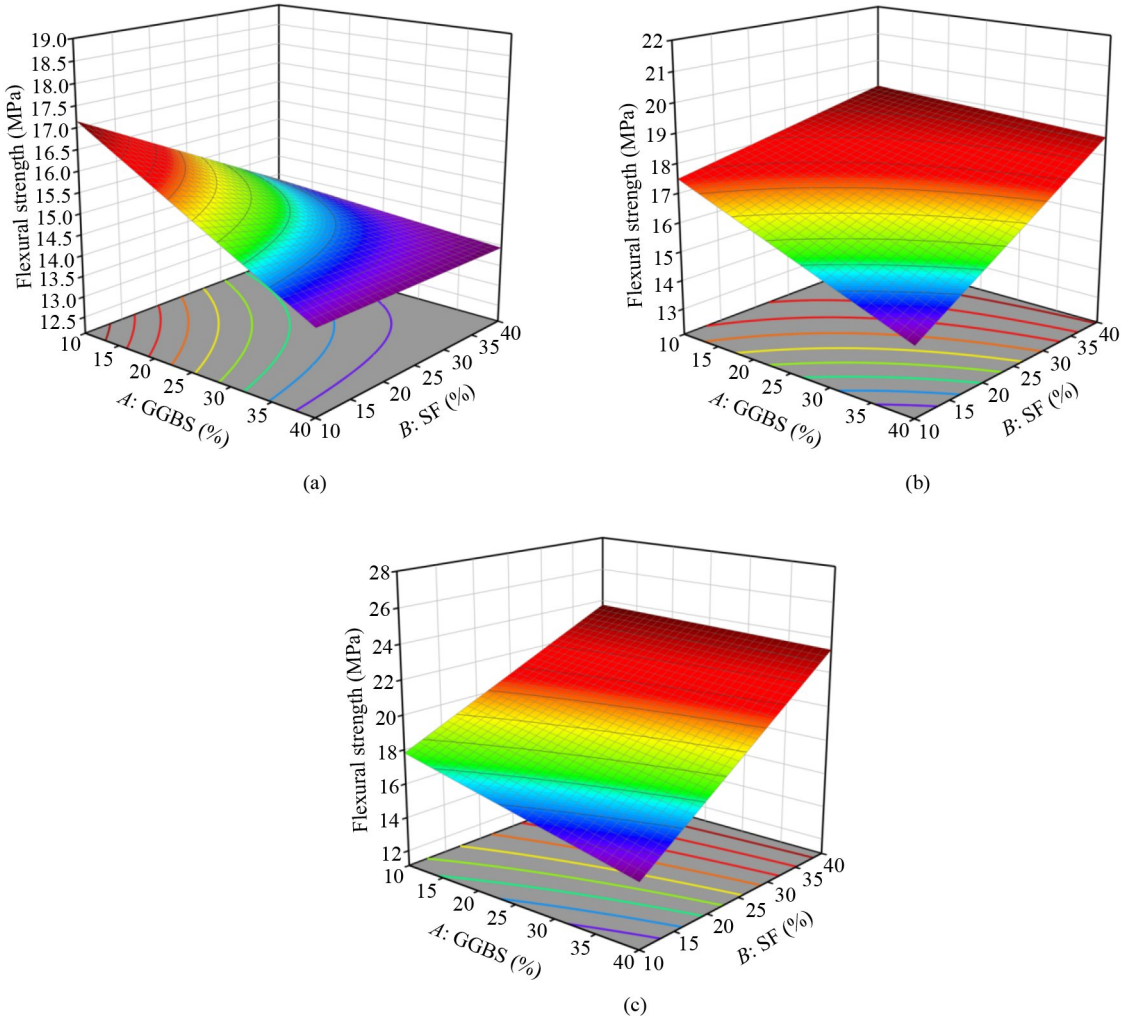



**Fig. 14** Flexural strength versus GGBS and SF at 1%, 2%, and 3% steel fiber: (a) at 1% steel fiber volume fraction; (b) at 2% steel fiber volume fraction; (c) at 3% steel fiber volume fraction.

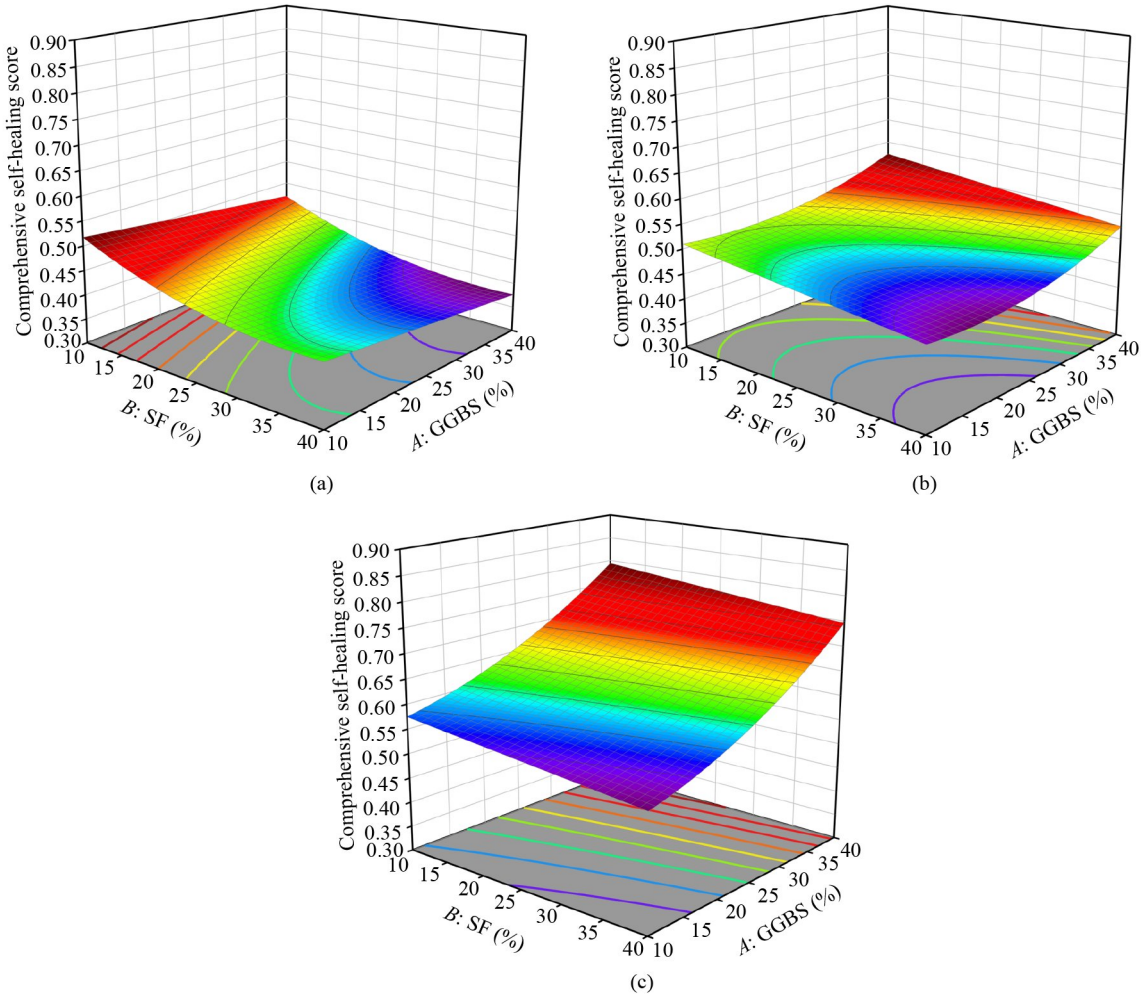



**Fig. 15** Comprehensive self-healing score versus GGBS and SF at 1%, 2%, and 3% steel fiber: (a) at 1% steel fiber volume fraction; (b) at 2% steel fiber volume fraction; (c) at 3% steel fiber volume fraction.

indicating that its marginal net contribution is limited after entropy weight-based comprehensive evaluation. This phenomenon may be attributed to the fact that mixtures with higher GGBS content tend to have relatively lower initial mechanical strength and higher matrix pore connectivity. After pre-damage, the generated cracks and micro-defects provide more direct channels for water ingress into the material interior, which sustains more continuous hydration during the healing period and thus results in more significant improvements in compressive strength recovery and overall densification-related indicators. In comparison, SF possesses high reactivity and is rapidly consumed in the early stage via micro-filling and pozzolanic reactions, leaving limited residual potential for sustained hydration in the later stage. As illustrated in Fig. 9, SF exerts a more prominent facilitating effect on flexural strength recovery but only a marginal positive impact on compressive strength recovery. Given that compressive performance-related indicators account for a larger proportion of the total weight in the comprehensive evaluation framework of this study, the advantages of SF in enhancing flexural recovery are partially offset when its contribution to net compressive recovery remains moderate. Therefore, this result does not imply that SF is ineffective for the self-healing of UHPC.

Based on the analysis of practical dosage ranges, the high-value regions of the comprehensive scores are mainly concentrated in the mix proportion combinations featuring high fiber content, high GGBS content, and low (or medium) SF content. This result indicates that enhancing the comprehensive self-healing performance in a tap water environment relies more on the crack control and bridging effects of fibers, as well as the late-stage reaction supply of GGBS. SF is more suitable as a regulatory variable for enhancing mechanical properties and interfacial densification, and its content needs to be controlled within a reasonable range to achieve overall synergy under the comprehensive objective.

### 3.6 X-ray diffraction phase analysis

After 90 d of full immersion curing in tap water, the XRD patterns of the deposits scraped from the crack areas of

pre-damaged flexural specimens in Groups R2, R13, R16, and R18 are presented in Fig. 16. The XRD patterns of all four groups are dominated by the characteristic peaks of Quartz, indicating that a small amount of quartz sand was inevitably entrained during the sampling process. Therefore, the results of this study focus more on identifying the main phase compositions of crack deposits and the phase differences between groups by means of XRD technology. In addition to Quartz, Calcite and a small amount of Portlandite (CH) were detected in all groups. This observation demonstrates that the self-healing products of UHPC cracks are closely associated with the dissolution-migration-reprecipitation process of $Ca^{2+}$ under water-saturated conditions [22,44,45]. Specifically, on the one hand, calcium-containing phases such as CH precipitate or remain in the crack regions; on the other hand, dissolved $CO_2$ in the environment participates in carbonation reactions to form calcium carbonate crystals that deposit in the cracks. Meanwhile, the continuous hydration of the matrix and the subsequent pozzolanic reactions of SCMs generate low-crystallinity calcium silicate hydrate (C-S-H) gels at the crack interfaces. The above multiple effects jointly promote the crack filling and densification process.

Among them, the characteristic peaks of Calcite and CH in Group R16 (without SF) are relatively more prominent, indicating that the pozzolanic consumption effect of SF on CH is weakened when SF is absent, making it easier for CH to precipitate and undergo subsequent carbonation deposition in the crack regions. In contrast, the CH characteristic peaks in Group R13 (with high dosages of both GGBS and SF) are relatively weak, which is highly consistent with the mechanism that reactive SCMs facilitate late-stage hydration reactions, consume CH and generate low-crystallinity C-S-H gels [18,37,46]. By comparison, the phase signals of the deposits in Group R2 (without GGBS) and Group R18 (with low dosages of both GGBS and SF) are generally weak, and their crack healing is characterized more by local carbonate deposition, with no prominent characteristics of cementitious phase products. In summary, the dosage of SF determines whether CH can be fully consumed, while GGBS exerts a more significant regulatory effect on the sustainability of late-stage hydration reactions. This conclusion is highly consistent with the RSM surface analysis results. The enhancement of compressive and flexural strengths mainly relies on the reinforcing effect of SF, whereas the development of

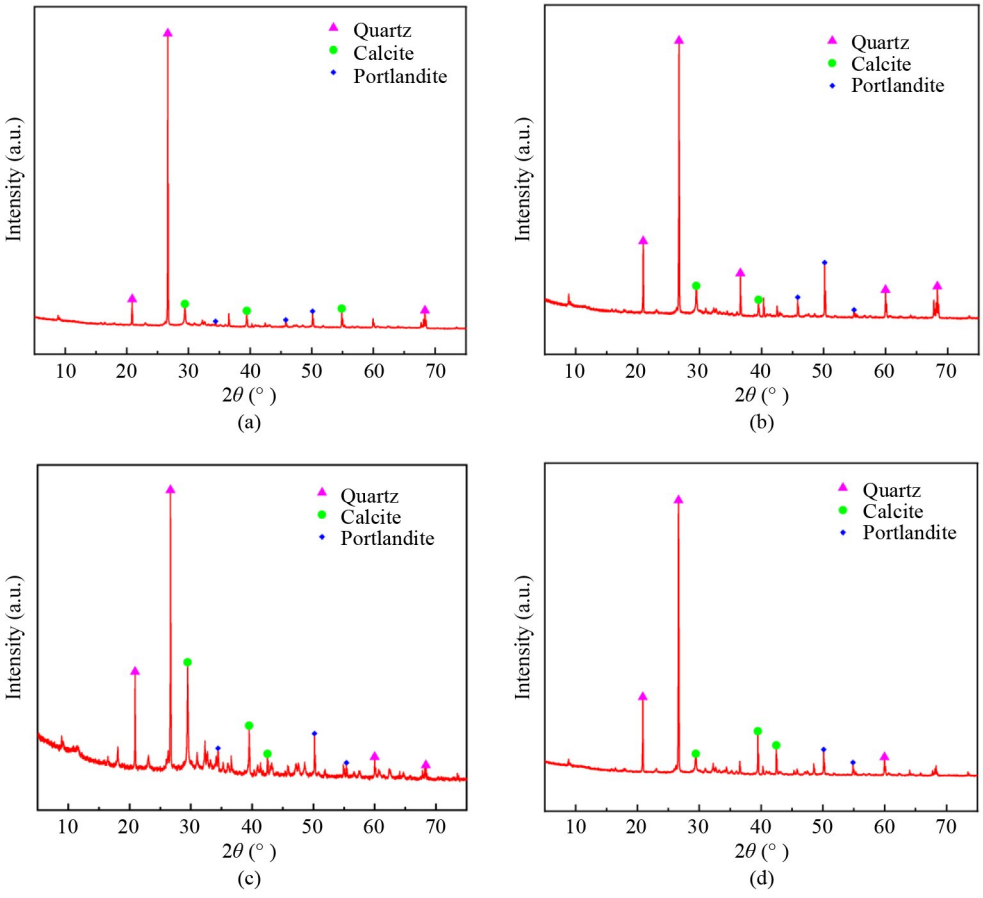



**Fig. 16** XRD patterns of the specimens: (a) R2: $A$ = 0, $B$ = 25, $C$ = 2; (b) R13: $A$ = 40, $B$ = 40, $C$ = 1; (c) R16: $A$ = 25, $B$ = 0, $C$ = 2; (d) R18: $A$ = 10, $B$ = 10, $C$ = 1.

long-term self-healing performance is more dependent on the continuous hydration contribution of GGBS. The results of this XRD analysis confirm from the perspective of phase composition that the crack self-healing process is jointly dominated by carbonate crystal deposition and secondary hydration product filling, and also provide microscopic support for the RSM models.

## 4 Conclusions

This study focused on the autogenous self-healing behavior of UHPC and employed RSM to quantify the effects of three key factors (GGBS, SF, and steel fibers) on self-healing performance. The main research conclusions are as follows.

The experimental results prove that the self-healing behavior of UHPC under water immersion conditions exhibits significant time dependence: the deposits on the crack surface gradually evolve from scattered dots in the early stage to banded continuous deposition morphology, and both the mechanical properties and non-destructive testing indicators present an overall upward trend with the extension of the healing age. Significant differences are also observed among groups with different mix proportions. The late-stage hydration reaction supply of SCMs and the bridging constraint effect of steel fibers jointly determine the reaction space and product filling efficiency at the cracks. Further verification via XRD phase identification confirms that the crack self-healing of UHPC is mainly dominated by the combined action of carbonate crystal deposition and secondary hydration product filling.

In terms of self-healing performance evaluation, multiple characteristic indicators were adopted to quantitatively characterize the differences in self-healing performance among groups with different mix proportions. The entropy weight method was introduced to realize the objective weighting and data fusion of multiple indicators, and a comprehensive scoring system for the unified evaluation of UHPC self-healing performance was established. This system integrates multi-dimensional information such as mechanical property recovery and ultrasonic integrity into a unified analysis framework. It not only avoids the evaluation deviation caused by a single focus on crack closure or strength recovery, but also reduces the interference of artificially assigned weights among indicators with different dimensions and fluctuation ranges, making the ranking results of different mix proportions more stable and interpretable. The results indicate that the mix proportion scheme featuring a high steel fiber volume fraction combined with a certain dosage of SF and GGBS possesses distinct advantages in terms of self-healing performance.

Finally, regression models capable of predicting the compressive strength, flexural strength, and comprehensive score of self-healing performance were established, realizing the quantitative expression of the relationship between mix proportion parameters and multi-performance responses. The results of statistical tests and residual diagnosis of the models demonstrate that all the established models have good fit and predictive ability. Analysis of the response surfaces reveals that increasing the steel fiber dosage exerts a significant enhancement effect on the compressive performance, flexural performance, and self-healing performance of UHPC. The mix proportion combination of high SF dosage coupled with low or medium GGBS dosage is more conducive to the improvement of compressive and flexural strengths. In contrast, the increase in GGBS dosage is more favorable for the improvement of the self-healing performance of specimens, and there exists an obvious synergistic effect between GGBS and steel fibers.

**Acknowledgements** This work was supported by the National Natural Science Foundation of China (Grant No. 52478235) and the National Key R&D Program of China (Nos. 2023YFB3711400 and 2025YFF0518600).

**Open Access** This article is licensed under a Creative Commons Attribution 4.0 International License, which permits use, sharing, adaptation, distribution and reproduction in any medium or format, as long as you give appropriate credit to the original author(s) and the source, provide a link to the Creative Commons licence, and indicate if changes were made. The images or other third party material in this article are included in the article's Creative Commons licence, unless indicated otherwise in a credit line to the material. If material is not included in the article's Creative Commons licence and your intended use is not permitted by statutory regulation or exceeds the permitted use, you will need to obtain permission directly from the copyright holder. To view a copy of this licence, visit http://creativecommons.org/licenses/by/4.0/.

**Competing interests** The authors declare that they have no competing interests.

## References

1. Shao X D, Deng L, Cao J H. Innovative steel-UHPC composite bridge girders for long-span bridges. Frontiers of Structural and Civil Engineering, 2019, 13(4): 981–989
2. Ahmed A, Uddin M N, Akbar M, Salih R, Khan M A, Bisheh H, Rabczuk T. Prediction of shear behavior of glass FRP bars-reinforced ultra-highperformance concrete I-shaped beams using machine learning. International Journal of Mechanics and Materials in Design, 2024, 20(2): 269–290
3. Shi C J, Wu Z M, Xiao J F, Wang D H, Huang Z Y, Fang Z. A review on ultra high performance concrete: Part I. Raw materials and mixture design. Construction and Building Materials, 2015, 101: 741–751

4. Jiang J Y, Zheng X J, Wu S P, Liu Z Y, Zheng Q. Nondestructive experimental characterization and numerical simulation on self-healing and chloride ion transport in cracked ultra-high performance concrete. Construction and Building Materials, 2019, 198: 696–709
5. Wang M, Du M F, Zhuang X Y, Lv H, Wang C, Zhou S. Multi-objective optimization of ultra-high performance concrete based on life-cycle assessment and machine learning methods. Frontiers of Structural and Civil Engineering, 2025, 19(1): 143–161
6. Zheng Q M, Li W T, Ren Q, Zhang H E, Dong B Q, Jiang Z W. A review on crack self-healing of ultra-high performance concrete and its active modulations. Bulletin of the Chinese Ceramic Society, 2025, 44(11): 3891–3902 (in Chinese)
7. Meraz M M, Mim N J, Mehedi M T, Bhattacharya B, Aftab M R, Billah M M, Meraz M M. Self-healing concrete: Fabrication, advancement, and effectiveness for long-term integrity of concrete infrastructures. Alexandria Engineering Journal, 2023, 73: 665–694
8. Ferrara L, Krelani V, Moretti F, Roig Flores M, Serna Ros P. Effects of autogenous healing on the recovery of mechanical performance of high performance fibre reinforced cementitious composites (HPFRCCs): Part 1. Cement and Concrete Composites, 2017, 83: 76–100
9. Kim M K, Kim D J, Chung Y S, Choi E. Direct tensile behavior of shape-memory-alloy fiber-reinforced cement composites. Construction and Building Materials, 2016, 102: 462–470
10. Zhou S, Jia Y, Wang C. Global sensitivity analysis for the polymeric microcapsules in self-healing cementitious composites. Polymers, 2020, 12(12): 2990
11. Minnebo P, Thierens G, De Valck G, Van Tittelboom K, De Belie N, Van Hemelrijck D, Tsangouri E. A novel design of autonomously healed concrete: Towards a vascular healing network. Materials, 2017, 10(1): 49
12. Yu X N, Zhang Q Y, Zhang X, Luo M. Microbial self-healing of cracks in cement-based materials and its influencing factors. Frontiers of Structural and Civil Engineering, 2023, 17(11): 1630–1642
13. Xi B, Al-Obaidi S, Ferrara L. Effect of different environments on the self-healing performance of Ultra High-Performance Concrete—A systematic literature review. Construction and Building Materials, 2023, 374: 130946
14. Vu-Bac N, Le-Anh T, Rabczuk T. A Machine Learning based uncertainty quantification for compressive strength of high-performance concrete. Frontiers of Structural and Civil Engineering, 2025, 19(5): 824–836
15. Zhu H L, Wu X, Luo Y L, Jia Y, Wang C, Fang Z, Zhuang X Y, Zhou S. Prediction of early compressive strength of ultrahigh-performance concrete using machine learning methods. International Journal of Computational Methods, 2023, 20(8): 2141023
16. Hung C C, El-Tawil S, Chao S H. A review of developments and challenges for UHPC in structural engineering: Behavior, analysis, and design. Journal of Structural Engineering, 2021, 147(9): 03121001
17. Kim S, Yoo D Y, Kim M J, Banthia N. Self-healing capability of ultra-high-performance fiber-reinforced concrete after exposure to cryogenic temperature. Cement and Concrete Composites, 2019, 104: 103335
18. Zheng Q M, Li C, Song F C, He B, Li W T, Jiang Z W. Autogenous self-healing of ultra-high-performance fiber-reinforced concrete with varying silica fume dosages: Secondary hydration and structural regeneration. Cement and Concrete Composites, 2023, 137: 104905
19. Zheng Q M, Yang E H, Li C, Ren Q, Zhang H, Song F C, Liu B, Jiang Z W. Influence of ultra-fine pozzolanic materials on the self-healing capabilities of ultra-high performance concrete under carbonation conditioning. Cement and Concrete Research, 2025, 187: 107712
20. Calvo J L G, Pérez G, Carballosa P, Erkizia E, Gaitero J J, Guerrero A. Development of ultra-high performance concretes with self-healing micro/nano-additions. Construction and Building Materials, 2017, 138: 306–315
21. Cuenca E, Mezzena A, Ferrara L. Synergy between crystalline admixtures and nano-constituents in enhancing autogenous healing capacity of cementitious composites under cracking and healing cycles in aggressive waters. Construction and Building Materials, 2021, 266: 121447
22. Xi B, Huang Z W, Al-Obaidi S, Ferrara L. Healing capacity of Ultra High Performance Concrete under sustained through crack tensile stresses and aggressive environments. Cement and Concrete Composites, 2024, 145: 105355
23. Yang Z X, Miao C X, Deng W Q, Liu D, Zhang J D, Gu J C. Multi-scale characterization of SAP impact on self-healing behavior in UHPC under varied crack widths and environments. Construction and Building Materials, 2024, 421: 135649
24. Beglarigale A, Eyice D, Tutkun B, Yazıcı H. Evaluation of enhanced autogenous self-healing ability of UHPC mixtures. Construction and Building Materials, 2021, 280: 122524
25. Xi B, Huang Z W, Al-Obaidi S, Ferrara L. Predicting ultra high-performance concrete self-healing performance using hybrid models based on metaheuristic optimization techniques. Construction and Building Materials, 2023, 381: 131261
26. Qin Y, Guan K, Kou J L, Ma Y B, Zhou H, Zhang X W. Durability evaluation and life prediction of fiber concrete with fly ash based on entropy weight method and grey theory. Construction and Building Materials, 2022, 327: 126918
27. Shi H W, Wang H Y, Xue S F, Feng S L, Li Y C. Durability evaluation of iron tailings concrete under freeze–thaw cycles and sulfate erosion based on entropy weighting method. Construction and Building Materials, 2024, 443: 137747
28. Lu Z, Feng Z G, Yao D D, Li X J, Ji H R. Freeze–thaw resistance of Ultra-High performance concrete: Dependence on concrete composition. Construction and Building Materials, 2021, 293: 123523
29. Li Z P, Lu D G, Gao X J. Optimization of mixture proportions by statistical experimental design using response surface method—A review. Journal of Building Engineering, 2021, 36: 102101
30. Song Y X, Wang X D, Li H C, He Y J, Zhang Z L, Huang J D. Mixture optimization of cementitious materials using machine learning and metaheuristic algorithms: State of the art and future prospects. Materials, 2022, 15(21): 7830
31. Abellan-Garcia J, Khan M I, Abbas Y M, Castro-Cabeza A,

Carrillo J. Multi-criterion optimization of low-cost, self-compacted and eco-friendly micro-calcium-carbonate- and waste-glass-flour-based ultrahigh-performance concrete. Construction and Building Materials, 2023, 371: 130793

32. Ferdosian I, Camões A. Eco-efficient ultra-high performance concrete development by means of response surface methodology. Cement and Concrete Composites, 2017, 84: 146–156
33. Wang X P, Yu R, Shui Z H, Song Q L, Zhang Z H. Mix design and characteristics evaluation of an eco-friendly Ultra-High Performance Concrete incorporating recycled coral based materials. Journal of Cleaner Production, 2017, 165: 70–80
34. Mosaberpanah M A, Eren O, Tarassoly A R. The effect of nano-silica and waste glass powder on mechanical, rheological, and shrinkage properties of UHPC using response surface methodology. Journal of Materials Research and Technology, 2019, 8(1): 804–811
35. Cappellesso V, Ferrara L, Gruyaert E, Van Tittelboom K, De Belie N. Resilient crystalline admixture in ultra-high performance self-healing concrete under cyclic freeze–thaw with de-icing salts. Cement and Concrete Research, 2024, 181: 107524
36. Abdellatief M, Abd Elrahman M, Elgendy G, Bassioni G, Tahwia A M. Response surface methodology-based modelling and optimization of sustainable UHPC containing ultrafine fly ash and metakaolin. Construction and Building Materials, 2023, 388: 131696
37. Jing R, Liu Y, Yan P Y. Uncovering the effect of fly ash cenospheres on the macroscopic properties and microstructure of ultra high-performance concrete (UHPC). Construction and Building Materials, 2021, 286: 122977
38. Zheng Q M, Xie Z C, Li J, Li W T, Jiang Z W. Autogenously self-healable cementitious composite incorporating autolytic mineral microspheres: Hydration regulation and structural alteration. Composites Part B: Engineering, 2023, 259: 110724
39. Chen Q, Li W T, Jiang Z W. Theoretical estimation of the elastic moduli of self-healing concrete relevant to the evolution of cracks closing due to crystallization- and precipitation-based mechanism. Journal of Building Engineering, 2022, 58: 104995
40. Luo X B, Xing G H, Qiao L, Miao P Y, Yu X G, Ma K Z. Multi-objective optimization of the mix proportion for dune sand concrete based on response surface methodology. Construction and Building Materials, 2023, 366: 129928
41. Wille K, Naaman A E, El-Tawil S, Parra-Montesinos G J. Ultra-high performance concrete and fiber reinforced concrete: Achieving strength and ductility without heat curing. Materials and Structures, 2012, 45(3): 309–324
42. Ahmad J, Kontoleon K J, Majdi A, Naqash M T, Deifalla A F, Ben Kahla N, Isleem H F, Qaidi S M A. A comprehensive review on the ground granulated blast furnace slag (GGBS) in concrete production. Sustainability, 2022, 14(14): 8783
43. Ji Y J, Cahyadi J H. Effects of densified silica fume on microstructure and compressive strength of blended cement pastes. Cement and Concrete Research, 2003, 33(10): 1543–1548
44. Van Tittelboom K, De Belie N. Self-healing in cementitious materials-A review. Materials, 2013, 6(6): 2182–2217
45. Li W T, Chen Q, Liu S F, Jiang Z W. Theoretical analysis of self-healing evolution of concrete with boundary moving due to carbonation. Journal of Building Engineering, 2024, 91: 109722
46. Elyasigorji F, Farajiani F, Manjili M H, Lin Q, Elyasigorji S, Farhangi V, Tabatabai H. Comprehensive review of direct and indirect pozzolanic reactivity testing methods. Buildings, 2023, 13(11): 2789